

Time-dependent generalized-active-space configuration-interaction approach to photoionization dynamics of atoms and molecules

S. Bauch,^{1,2} L. K. Sørensen,^{1,2} and L. B. Madsen¹¹*Department of Physics and Astronomy, Aarhus University, Aarhus 8000 C, Denmark*²*Institut für Theoretische Physik und Astrophysik, Christian-Albrechts-Universität zu Kiel, Leibnizstraße 15, 24098 Kiel, Germany*

(Received 9 October 2014; published 9 December 2014)

We present a wave-function-based method to solve the time-dependent many-electron Schrödinger equation with special emphasis on strong-field ionization phenomena. The theory builds on the configuration-interaction (CI) approach supplemented by the generalized-active-space concept from quantum chemistry. The latter allows for a controllable reduction in the number of configurations in the CI expansion by imposing restrictions on the active orbital space. The method is similar to the recently formulated time-dependent restricted-active-space CI method [D. Hochstuhl and M. Bonitz, *Phys. Rev. A* **86**, 053424 (2012)]. We present details of our implementation and address convergence properties with respect to the active spaces and the associated account of electron correlation in both ground-state and excitation scenarios. We apply the time-dependent generalized-active-space CI theory to strong-field ionization of polar diatomic molecules and illustrate how the method allows us to uncover a strong correlation-induced shift of the preferred direction of emission of photoelectrons.

DOI: [10.1103/PhysRevA.90.062508](https://doi.org/10.1103/PhysRevA.90.062508)

PACS number(s): 31.15.-p, 32.80.Fb, 33.80.Eh

I. INTRODUCTION

Tracing electron motion and correlation on their natural time scales has become possible within the past decade due to enormous experimental progress in light-pulse technology and detection methods [1–4]. These experimental advancements and associated new possibilities for elucidating quantum motion on an ultrafast time scale challenge theory. Clearly, approaches that treat electron correlation and at the same time are explicitly time dependent are needed to fully exploit the potential of the experimental capabilities. The development and application of such a time-dependent (TD) quantum theory for the many-electron problem (MEP) including a possibly strong external field is the topic of the present work.

Over the years, various approaches for the solution of the TDMEP on a quantum-mechanical level have been proposed and applied. On the one hand, there exist approximative methods which consider a reduced number of electrons (typically one or two) in precalculated pseudopotentials created by frozen electrons that are assumed to be inactive in the considered dynamics, apart from contributing to the potential governing the motion of the active electrons. This approach results in the single- and two-active-electron (SAE and TAE) approximations for which the TD Schrödinger equation (TDSE) has been solved for photoionization, high-order harmonic generation (HHG), and related phenomena since the late 1980s [5]. The appeal of these methods is their flexibility and numerical feasibility with respect to the considered systems. The dynamical effects of the frozen electrons, however, cannot be tested within these SAE and TAE approximations, and likewise there is no explicit account of electron correlation in general. To this end, approaches have been developed where all electrons are treated simultaneously on different levels of “activity.” Numerical tractable methods are either achieved by approximating the electron-electron (e - e) interactions or by reducing the configuration space. Among these methods are the time-dependent configuration-interaction (TD-CI) method and its truncations, where, in particular, the simplest TD-CI-singles (TD-CIS) with only single-orbital excitation out of

the Hartree-Fock (HF) ground state has been applied [6,7]. In addition, we mention the TD density functional theory [8], TD natural orbital theory [9], TD coupled-cluster theory [10], the nonequilibrium Green’s functions approaches [11–13], and the state-specific expansion approach [14,15]. Up to now, in particular, the TD R -matrix theory [16–19] and the multiconfigurational time-dependent Hartree-Fock (MCTDHF) method [13,20–25] have found applications in the photoionization community. In the perturbative regime for the matter-light interaction, the MCTDHF method has been applied to the determination of inner-shell photoionization cross sections for molecular hydrogen fluoride [25]. The number of configurations in the MCTDHF method increases exponentially with respect to the number of electrons due to the full-CI expansion. This makes the method infeasible for systems having more than a few electrons interacting with a strong field. The TD complete-active-space self-consistent-field method (TD-CASCF) [26] and the more general TD restricted-active space SCF (TD-RASSCF) [27–29] cure this scaling by imposing restrictions on the active orbital spaces, while keeping the attractive SCF notion of the MCTDHF approach; i.e., the orbitals are TD and optimally updated in each time step.

In this paper, we consider the TD generalized-active-space (GAS) CI concept, which is based on a general CI truncation scheme adapted from (time-independent) quantum chemistry. In the GAS (or RAS) approach [30,31] the single-particle basis is partitioned into physically motivated subsets and only the configurations that are expected to be most relevant for the processes under consideration are included in the CI expansion, thus reducing the number of configurations considerably. By specifying the GAS, generalizations of the SAE and TAE approximations, without the need of constructing pseudopotentials, are readily obtained as limiting cases. Moreover, CI truncations, such as CIS, CIS-doubles (CISD), CISD-triples (CISDT), etc., can be easily specified and the method, accordingly, allows a straightforward increase in the account of electron correlation within a specified active orbital

space. The present method is similar to the time-dependent restricted-active-space (TD-RAS) CI scheme [32], which was applied to calculate the photoionization cross sections of beryllium and neon [33].

A fundamental problem of any truncated CI method is the choice of a good orbital basis. In this work, we address this issue with the focus on TD excitations and give a detailed analysis of different choices: pseudo-orbitals based on HF orbitals similar to [32], an adapted version for larger systems, and natural orbitals. Further, we demonstrate in the limiting case of four electrons the convergence of the method by detailed comparison with fully correlated TDSE or equivalent calculations. In addition, we give details of the implementation and extend the approach to small molecules in strong external fields. In particular, the approach allows us to uncover a strong effect of electron correlation on the preferred emission direction of photoelectrons.

The paper is organized as follows. Section II outlines the concepts of CI and GAS and introduces the equations of motion and notations used in this work. In Sec. III, we address the problem of photoionization and the related choice of appropriate orbital basis sets. Here we choose a partially rotated basis, which combines orbital and grid-based approaches in an efficient manner. In Sec. IV, we apply the TD-GASCI method to model systems for atomic helium and beryllium and compare with fully correlated results. We especially focus on convergence properties with respect to the GAS partitions and the choice of orbitals. Our analysis covers ground-state properties as well as excitation scenarios. Finally, the application of TD-GASCI is extended to molecular systems. We focus on the polar diatomic lithium-hydride (LiH) molecule. After a discussion of its ground-state properties, we present a study of the strong-field ionization with single-cycle laser pulses including electron correlation effects. Section V summarizes and concludes.

II. THEORY

We aim to provide a general scheme for the numerical treatment of the nonrelativistic many-electron TDSE (ME-TDSE), which is particularly well suited for the description of ionization processes of atoms and molecules by short and/or strong pulses.

The fundamental equation is the TDSE for N_{el} electrons in an atom or a molecule with fixed nuclei (atomic units are used throughout),

$$i \frac{\partial}{\partial t} |\Psi(t)\rangle = \hat{H}(t) |\Psi(t)\rangle, \quad (1)$$

with the TD Hamiltonian

$$\hat{H}(t) = \sum_{i=1}^{N_{el}} \hat{h}_i(t) + \sum_{i<j}^{N_{el}} \hat{w}_{ij}. \quad (2)$$

The single-particle term referring to particle i ,

$$\hat{h}_i(t) = \hat{t}_i + \hat{v}_i + \mathbf{F}(t) \hat{\mathbf{r}}_i, \quad (3)$$

consists of the kinetic energy \hat{t}_i , the potential describing the attractive interaction with the nuclei \hat{v}_i , and the interaction with the external field, $\mathbf{F}(t) \hat{\mathbf{r}}_i$. The latter being described

in the dipole approximation within the length gauge. The two-body part of $\hat{H}(t)$ is given by the binary interaction between electrons i and j , \hat{w}_{ij} .

The general solution of Eq. (1) is only feasible by employing powerful numerical techniques. Pioneering work in the context of (strong-field) ionization was done for (effective) one-electron systems in Refs. [5,34–36]. For systems with interacting electrons, only very few cases are manageable without approximations, such as helium and H_2 [37–45], and even in these cases the whole range of laser frequencies and intensities cannot be accessed.

When the number of electrons increases, only approximate solutions are accessible (see, e.g., Ref. [46] for a thorough review), and it is mandatory to go beyond the level of time-dependent Hartree-Fock (TDHF) to allow for a description of e - e correlation effects.

A. Time-dependent configuration interaction

Let us form Slater determinants $|\Phi_I\rangle$ from the spin orbitals $|\phi_i\rangle = |\varphi_i\rangle \otimes |\sigma\rangle$ to construct the many-electron basis. Here $|\sigma\rangle$ with $\sigma = \{\alpha, \beta\}$ denotes the spin degree of freedom and $|\varphi_i\rangle$ denotes the remaining single-particle degrees of freedom. The multi-index I specifies the individual configurations spanning the full CI Fock space \mathcal{V}_{FCI} . The expansion of $|\Psi(t)\rangle$ into this basis set with TD coefficients $C_I(t)$,

$$|\Psi(t)\rangle = \sum_{I \in \mathcal{V}_{FCI}} C_I(t) |\Phi_I\rangle, \quad (4)$$

gives the matrix form of the TDSE,

$$i \frac{\partial}{\partial t} C_I(t) = \sum_{J \in \mathcal{V}_{FCI}} H_{IJ}(t) C_J(t), \quad (5)$$

with $H_{IJ}(t) = \langle \Phi_I | \hat{H}(t) | \Phi_J \rangle$. The matrix representation of $\hat{H}(t)$ is referred to as the CI-matrix in the following.

The CI-matrix elements are conveniently determined using the language of second quantization. In the occupation number representation $|\mathbf{n}\rangle$ and $|\mathbf{m}\rangle$, the matrix elements are then given by [47]

$$\begin{aligned} \langle \mathbf{n} | \hat{H} | \mathbf{m} \rangle &= \sum_{pq} h_{pq}(t) \sum_{\sigma} \langle \mathbf{n} | \hat{c}_{p\sigma}^{\dagger} \hat{c}_{q\sigma} | \mathbf{m} \rangle \\ &+ \frac{1}{2} \sum_{pqrs} w_{pqrs} \sum_{\sigma\tau} \langle \mathbf{n} | \hat{c}_{p\sigma}^{\dagger} \hat{c}_{r\tau}^{\dagger} \hat{c}_{s\tau} \hat{c}_{q\sigma} | \mathbf{m} \rangle, \end{aligned} \quad (6)$$

where a spin-free Hamiltonian, i.e., the same spatial orbital for α and β spin is assumed, and where $\hat{c}_{p\sigma}$ ($\hat{c}_{p\sigma}^{\dagger}$) denotes the annihilation (creation) operator of the spin orbital $|\varphi_p\rangle \otimes |\sigma\rangle$. Here, the *one-electron* integrals,

$$h_{pq} = t_{pq} + v_{pq}(t), \quad (7)$$

of the kinetic and potential energy contributions to the single-particle part are given by

$$\begin{aligned} t_{pq} &= -\frac{1}{2} \int d\mathbf{r} \varphi_p^*(\mathbf{r}) \nabla^2 \varphi_q(\mathbf{r}), \\ v_{pq}(t) &= \int d\mathbf{r} \varphi_p^*(\mathbf{r}) v(\mathbf{r}; t) \varphi_q(\mathbf{r}), \end{aligned} \quad (8)$$

with $v(\mathbf{r}; t) = v(\mathbf{r}) + \mathbf{F}(t)\mathbf{r}$, and the *two-electron* integrals of the interaction by (note that we use chemist notation of the integrals [47])

$$w_{pqrs} = \iint d\mathbf{r}_1 d\mathbf{r}_2 \varphi_p^*(\mathbf{r}_1) \varphi_r^*(\mathbf{r}_2) w(\mathbf{r}_1, \mathbf{r}_2) \varphi_q(\mathbf{r}_1) \varphi_s(\mathbf{r}_2). \quad (9)$$

Especially the nature of the two-electron integrals (9) imposes practical restrictions on the underlying single-particle basis, since for general basis sets the number of matrix elements scales as $O(N_b^4)$ with N_b being the number of spatial orbitals $\varphi_i(\mathbf{r})$ [corresponding to $2N_b$ spin orbitals $\phi_i(z)$, $z = (\mathbf{r}, \sigma)$]. A way to cure this unfavorable scaling in the context of photoionization-related problems, which involves the electronic continuum and hence necessarily a large N_b , is described in Sec. III.

Up to this point, Eq. (5) is exact and inherits the full complexity of the MEP, and the approach is referred to as full CI (FCI). The number of configurations n_{conf} [or number of Slater determinants in Eq. (4)] spanning \mathcal{V}_{FCI} scales as

$$n_{\text{conf}} = \binom{2N_b}{N_{\text{el}}}. \quad (10)$$

In principle, a reduction by some factor by exploiting symmetries of the system, such as spin and spatial symmetries, is possible [46]. In the following, we assume conservation of the total spin for our spin-independent Hamiltonian (2) and (3). Still FCI calculations are only feasible for a very limited number of spin orbitals $2N_b$ and few electrons [48,49] and therefore are mostly used to benchmark other approximative methods.

To overcome this fundamental barrier, the CI expansion (4) has to be truncated at a certain level. Frequently used are CIS, CISD, and so on, in which one takes into account only singly, doubly, or higher excited determinants with the hope to capture the dominant correlation contributions. Especially in the context of photoionization and related phenomena, the truncation at the singles level has some tradition [6,7,50–57], since photoionization into a structureless continuum can often be described accurately in a single-electron picture.

In this work, we take a more general approach by partitioning the single-particle basis into physically motivated subsets and choosing determinants that are expected to be most relevant for the processes under consideration. This concept is known as generalized (or restricted) active space (GAS or RAS) in the quantum chemistry literature [30,31]. A TD realization based on a time-independent spin-orbital basis was presented in Ref. [32] and in an SCF setting in Refs. [27–29]. The idea of selecting determinants by their importance, and thus truncating the CI expansion, has a long tradition in atomic and molecular physics [58].

B. GAS scheme

The configuration space is determined by two arrays of numbers. The first array, N_b , contains information about the partition of the single-particle spin-orbital basis into the G subspaces of the GAS. We may order the single-particle basis in any desired way. For the present discussion it is convenient to assume that the spin orbitals are ordered according to their

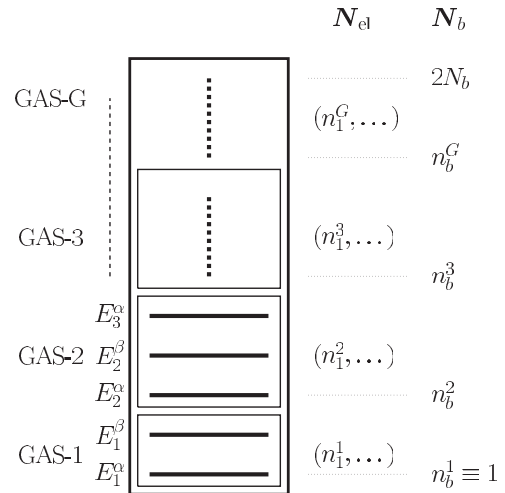


FIG. 1. Schematic of the generalized-active-space (GAS) method with G subspaces GAS-1 to GAS- G . The spin-orbital partition is given by $N_b = [1, n_b^2, \dots]$ and the allowed number of electrons in each subspace by $N_{\text{el}} = [(n_1^1, \dots), \dots, (n_1^G, \dots)]$. The energy eigenvalues of the single-particle orbitals are labeled by $E_1^{\alpha,\beta}$, where α and β denote the spin coordinate. For the nonrelativistic studies in this work, these are degenerate, $E_i^\alpha = E_i^\beta$.

energy. The lowest orbital is indexed by 1, the next (possibly degenerate) by 2, etc., until the highest-lying spin orbital, which is indexed by $2N_b$, the total number of spin orbitals. The notation $n_b^1 = 1$ means that subspace 1 in the GAS partitioning contains spin orbitals from the lowest one, 1. Then n_b^2 denotes the value of the spin-orbital index for the lowest-lying spin orbital in the second subspace, n_b^3 the index of the lowest-lying spin orbital in the third subspace, and so forth (Fig. 1). This information is summarized in N_b , containing the string of indices

$$N_b = [n_b^1 \equiv 1, n_b^2, \dots, n_b^G]. \quad (11)$$

The second array specifies the number of occupied spin orbitals that we allow in each subspace of the GAS partitioning,

$$N_{\text{el}} = [(n_1^1, n_2^1, \dots), \dots, (n_1^G, n_2^G, \dots)]. \quad (12)$$

As an illustrative, but not practical, relevant example, consider a single-particle basis with only six spin orbitals corresponding to three different spatial orbitals and three different energies for a two-electron system, which are degenerate with respect to spin projection. Let $G = 2$, such that we have two active subspaces denoted by GAS-1 and GAS-2. Assume we choose the first subspace to include only the two lowest degenerate spin orbitals and the second to include the remaining four. In this case $N_b = [n_b^1 = 1, n_b^2 = 3]$. The specification of N_{el} determines the amount of correlation that is taken into account between these orbitals. For example, we could consider $N_{\text{el}} = [(n_1^1 = 2, n_2^1 = 1), (n_1^2 = 0, n_2^2 = 1)]$, which allows two or one occupied orbital in GAS-1 and zero or one occupied orbital in GAS-2. The set of occupation numbers with subscript 1, i.e., the combination $[(n_1^1 = 2), (n_2^1 = 0)]$, corresponds to configurations with both lowest-lying spin orbitals occupied in the lowest subspace, GAS-1, and no occupied spin orbitals in the other subspace, GAS-2. The other set of occupation numbers with subscript 2, i.e., the combination $[(n_2^2 = 1), (n_2^1 = 1)]$,

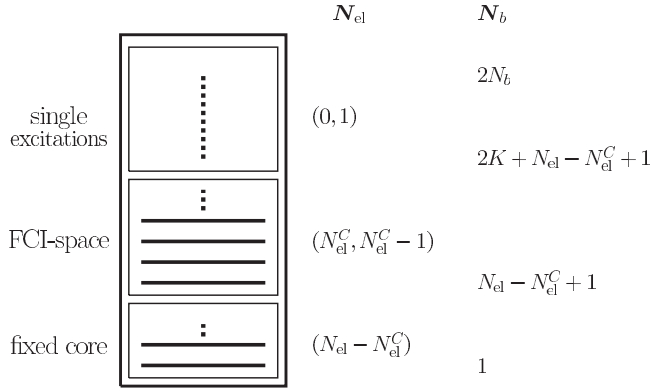


FIG. 2. Schematic of the GAS partitioning mainly used in this work. The scheme is denoted by $\text{CAS}^*(N_{\text{el}}^C, K)$ and consists of a fixed core with $N_{\text{el}} - N_{\text{el}}^C$ electrons in the same number of spin orbitals (this space is empty if $N_{\text{el}}^C = N_{\text{el}}$) and an active space with N_{el}^C electrons in $2K$ spin orbitals, from which one electron can be removed and excited into GAS-G describing the one-electron continuum.

describes one-particle excitation out of GAS-1 into GAS-2. In both cases, $\sum_j^G n_i^j = N_{\text{el}}$ for all i , as it should be. If we had chosen $N_{\text{el}} = [(n_1^1 = 2, n_2^1 = 1, n_3^1 = 0), (n_1^2 = 0, n_2^2 = 1, n_2^2 = 2)]$, we would have included double excitation out of GAS-1 (doubles) in addition to the singles of the previous example. It is clear that such partitioning in the general case allows the realization of any excitation scheme. It is also clear that the introduction of restrictions on the excitation between the different GASs dramatically reduce n_{conf} .

In the context of this work, we focus mainly on excitation phenomena with one-electron continua, i.e., excitations, where we allow one electron to be removed from the bound-state part of the spectrum, described, for example, by the GAS-1, GAS-2, and GAS-3 in Fig. 1 and excited to the GAS describing the continuum, GAS-G. To relate to the commonly used notation in quantum chemistry, we denote this case by $\text{CAS}^*(N_{\text{el}}^C, K)$. Here CAS refers to “complete-active-space,” N_{el}^C denotes the number of electrons in the active space, and K is the number of single-particle spatial orbitals in the active space. Finally, the star indicates that single excitations out of the active space have been added compared to the usual CAS scheme (sometimes also written as $[N_{\text{el}}^C, K]$ -CAS [59]).

The CAS^* scheme is illustrated in Fig. 2. The lowest GAS-1 describes a fixed core with $N_{\text{el}} - N_{\text{el}}^C$ electrons, where each electron occupies one spin orbital. This space is empty if one chooses to include all electrons in the active space, corresponding to the specification $\text{CAS}^*(N_{\text{el}}, K)$. GAS-2 is the active space with N_{el}^C electrons occupying $2K$ spin orbitals, for which all possible configurations are constructed, and in this sense a FCI description is maintained in this space. On top of that, we allow for single excitations from GAS-2 to GAS-3; i.e., we remove one electron from GAS-2, resulting in $N_{\text{el}}^C - 1$ electrons in GAS-2, and create it in GAS-3. The number of electrons in the individual subspaces and the corresponding partition of the single-particle spin-orbital basis are given in Fig. 2, right columns. Although some of the electrons may be kept frozen within the GAS scheme, i.e., some spin orbitals are always occupied, we emphasize that their interaction potential with all other electrons contributes to the sum in

the Hamiltonian (6) and no pseudopotentials for the explicitly active electrons need to be set up.

Using the GAS concept, the CI expansion (4) reduces in size,

$$|\Psi^{\text{GAS}}(t)\rangle = \sum_{I \in \mathcal{V}_{\text{GAS}}} C_I(t) |\Phi_I\rangle, \quad (13)$$

where only configurations within the specified Fock space \mathcal{V}_{GAS} contribute. The corresponding set of differential equations for the amplitudes reads

$$i \frac{\partial}{\partial t} C_I(t) = \sum_{J \in \mathcal{V}_{\text{GAS}}} H_{IJ}^{\text{GAS}}(t) C_J(t). \quad (14)$$

All limiting cases for CI calculations, such as SAE, CIS, CISD, etc., up to FCI can be realized by the appropriate GAS scheme [32].

The solution of Eq. (14) requires a choice of a single-particle spin-orbital basis $|\varphi_i\rangle \otimes |\sigma\rangle$, which allows for an efficient GAS expansion in terms of Slater determinants. Once the single-particle basis is constructed and the one- and two-electron integrals, Eqs. (8) and (9), respectively, are evaluated, the GASCI matrix $H_{IJ}^{\text{GAS}}(t)$ can be calculated. A straightforward way to evaluate Eqs. (8) and (9) is to apply Slater-Condon rules [47], but this approach is in practice limited to a rather small determinantal space due to the high degree of sparsity of the Hamiltonian and the unavoidable “calculation” of zero elements in $H_{IJ}^{\text{GAS}}(t)$. An alternative efficient way already proposed in the 1980s in the original formulation of RAS-CI [30] overcomes the latter problem by decomposing the excitations into α and β spin strings and employing a lexicographical ordering of the determinants. This approach was also taken in Ref. [32], and variations thereof were taken in Refs. [27–29]. In this work, we use a generalized scheme based on the construction and manipulation of *types* of excitation classes, which is particularly suited for GAS calculations and which has previously been successfully applied in coupled-cluster theory [60,61]. In this approach the zero parts of the CI matrix are identified and omitted from the calculation and only the remaining nonzero blocks are calculated and stored in a sparse matrix format. Besides, the scheme offers a very efficient way of setting up the CI matrix with a minimal number of evaluation of the electron integrals and provides a strategy for parallelization. Additional information and a detailed description of the reformulated integral direct method and algorithm is to be found in a forthcoming publication [62].

C. Time propagation

To solve Eq. (14), we first set up $H_{IJ}^{\text{GAS}}(t)$. The solution of Eq. (14) is given by discretization of the time variable $t = N_t \Delta t$ into N_t time steps and successive application of the time-evolution operator $U(t, t + \Delta t) = \exp[-iH(t + \Delta t)\Delta t]$ to the vector of coefficients $C_I(t)$. In order to avoid a diagonalization of the (large) CI matrix $H_{IJ}^{\text{GAS}}(t)$ at each time step, we employ an Arnoldi-Lanczos procedure and propagate the matrix equation in the corresponding Krylov subspace (we typically use a Krylov dimension of 10), which results in a unitary and stable propagation scheme. Details of the time-propagation algorithm can be found in Refs. [63,64].

This method involves only matrix multiplications of $H_{IJ}^{\text{GAS}}(t)$ with the coefficient vector $C_I(t)$, often referred to as the “ σ -vector step” in the CI literature [31], and can be performed efficiently using sparse matrix algebra and by exploiting block structures of the CI matrix. The initial condition $|\Psi^{\text{GAS}}(t=0)\rangle \equiv |\Psi_0^{\text{GAS}}\rangle$ for Eq. (13) [or $C_I(t=0) \equiv C_I^0$ for Eq. (14)] is prepared through imaginary time propagation (ITP) by replacing $t \rightarrow it$; see, e.g., Refs. [65,66]. To obtain the correctly correlated initial state, it is crucial to use exactly the same parameters with respect to the single-particle basis and the GASCI scheme as in the real time propagation.

III. BASIS SETS

In this section, we discuss the spatial part of the single-particle basis functions. For the convergence of truncated CI expansions, the choice of the single-particle basis plays a crucial role. Roughly speaking, the single-particle basis used to form the Slater determinants for the many-particle basis should closely resemble the physical one- and many-electron excitations of the system. For ground-state CI calculations, it can be shown that the CI expansion converges fastest using natural orbitals [67]. The most common approach is the use of HF reference states or improved orbitals which incorporate part of the e - e correlation contribution on the single-particle level. However, all of these orbital-based expansions with good properties for the ground- and bound-state CI expansions become essentially inapplicable in the limit of spatially extended systems. This is caused by the highly unfavorable scaling of the two-electron integrals with the number of single-particle basis functions, $O(N_b^4)$.

A. Partially rotated basis

In order to allow for photoionization processes with large computational grids, we follow a different strategy [32] and use a partially rotated [68] basis set. In the following, we work out the formulas for the one-dimensional (1D) case. Analogous expressions in 3D spherical coordinates [46] or prolate spheroidal coordinates [69] are straightforward and pose no conceptual difficulties. In short, the technique can be summarized by using localized HF-like orbitals for the description of the bound part of the spectrum and a gridlike representation for the continuum part. A similar technique was developed in Ref. [70].

Let us consider a single-particle basis composed of finite-element discrete-variable representation (FE-DVR) functions [71]. Similar expressions and strategies can be developed, e.g., with B splines [72]. The FE-DVR basis consists of N_e elements, which discretize the simulation box ranging from $[-x_s, x_s]$ into partitions,

$$-x_s = x^0 < \dots < x^i < x^{i+1} < \dots < x^{N_e} = x_s. \quad (15)$$

Each element, $[x^i, x^{i+1}]$, is spanned by n_g DVR functions. The basis functions are given by (we follow the notation in Refs. [11,73])

$$\chi_m^i = \frac{f_{n_g-1}^i(x) + f_0^{i+1}(x)}{\sqrt{w_{n_g-1}^i + w_0^{i+1}}} \quad \text{for } m = 0 \text{ (bridge)}, \quad (16)$$

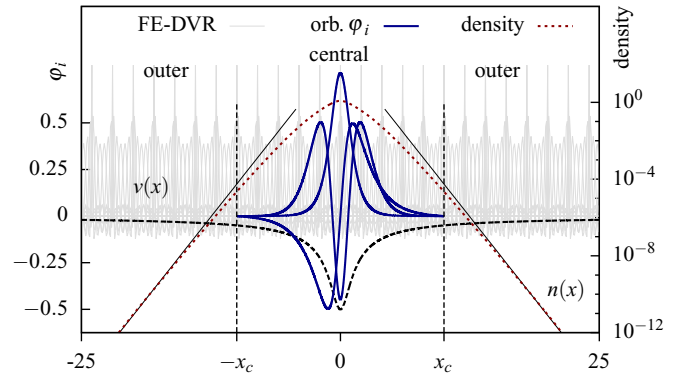


FIG. 3. (Color online) Schematic view of the partially rotated basis set with pseudo-orbitals ϕ_i in the central region $[-x_c, x_c]$ (solid blue lines) close to the minimum of the binding potential (dashed black line). In addition, a correlated single-particle density, cf. Eq. (34), for the ground state of a model for beryllium (see Sec. IV B) calculated for the complete computational grid $[-x_s, x_s]$ is given by the dashed red line (logarithmic scale to the right). The asymptotics is indicated by the thin black lines labeled “ $n(x)$ ”; cf. Eq. (26). The underlying FE-DVR grid (all functions are included in the calculation) is sketched in gray. Parameters in the figure are $x_s = 30$ and $x_c = 10$. We used 30 elements with eight DVR functions per element. Quantities on the abscissa are given in atomic units (a.u.).

$$\chi_m^i = \frac{f_m^i(x)}{\sqrt{w_m^i}} \quad \text{else (element)}, \quad (17)$$

with the Lobatto shape functions

$$f_m^i(x) = \prod_{\bar{m} \neq m} \frac{x - x_{\bar{m}}^i}{x_m^i - x_{\bar{m}}^i} \quad (18)$$

and the Gauß-Lobatto quadrature points x_m^i and weights w_m^i . The lower index m labels the DVR function and the upper index i the corresponding element. The bridge functions (16) connect adjacent elements i and $i+1$ and assure communication between both elements and the continuity of the wave function. The overall basis is schematically drawn in Fig. 3 with gray lines. The bridge functions (16) have spiky shape.

The FE-DVR matrix elements of Eqs. (8) and (9) possess a simple form [11,71,74],

$$v_{pq} = v(x_p) \delta_{pq}, \quad (19)$$

$$w_{pqrs} = w(x_p, x_r) \delta_{pq} \delta_{rs}, \quad (20)$$

$$t_{pq} \equiv t_{m_1 m_2}^{i_1 i_2} = \frac{(\delta_{i_1 i_2} + \delta_{i_1 i_2 \pm 1})}{2} \int dx \left(\frac{d}{dx} \chi_{m_1}^{i_1}(x) \right) \left(\frac{d}{dx} \chi_{m_2}^{i_2}(x) \right), \quad (21)$$

where we combined element indices i and DVR function indices m to multi-indices p, q, r, s , in analogy to Eqs. (8) and (9). We point out that the number of nonvanishing two-electron integrals (20) scales as $O(N_b^2)$, and not $O(N_b^4)$ as for arbitrary sets, which is of high practical importance for the present approach.

Unfortunately, a single Slater determinant constructed directly from the FE-DVR functions represents a poor reference state for the CI expansion. We therefore follow Ref. [32] and partition the basis set interval $[-x_s, x_s]$ into a central part $[-x_c, x_c]$ close to the nuclei and a remaining outer part for $|x| > x_c$; cf. Fig. 3. The partition point x_c is chosen such that it coincides with an FE-DVR element partition x^i between elements i and $i + 1$. The FE-DVR basis set is thus partitioned as

$$\begin{aligned}\chi_p^c(x) &\equiv \chi_m^j(x) \forall j, m : x_m^j \in (-x_c, x_c) \text{ [central]}, \\ \chi_p^o(x) &\equiv \chi_m^j(x) \text{ else [outer]}.\end{aligned}\quad (22)$$

Note that the division of space into an inner and an outer region is also central in (TD) R -matrix theory [16–19,75].

In the following $\varphi_k(x)$ [$\varphi_k^o(x)$] denotes an orbital localized in the central (outer) region. For $x \in (-x_c, x_c)$, orbitals (solid blue lines in Fig. 3) with good reference properties, such as HF orbitals, are constructed; cf. Sec. III B. In terms of the FE-DVR functions, these are expressed as

$$\begin{aligned}\varphi_k(x) &= \sum_l b_{lk}^c \chi_l^c(x) \quad \text{with} \quad (23) \\ b_{lk}^c &= \int_{-x_c}^{x_c} \varphi_k(x) \chi_l^c(x) dx.\end{aligned}\quad (24)$$

By excluding the bridge functions connecting the central with the outer region $|x| > x_c$ from the basis set in $(-x_c, x_c)$, all orbitals are zero at $|x| = x_c$ by construction; i.e., $\varphi_k(x) \equiv 0$ for $|x| > x_c$. In particular, $\varphi_i(x) \perp \varphi_j(x)$ and $\varphi_i(x) \perp \varphi_p^o(x) = \chi_p^o(x)$ holds. The matrix elements are thus transformed by the matrix b^c from Eq. (24).

Returning to the whole grid of $[-x_s, x_s]$, i.e., including all functions φ^o and the bridge functions at $\pm x_c$ into the basis set, this transformation is continued such that the outer part remains unchanged,

$$b = \begin{pmatrix} \mathbf{1} & \\ & b^c \\ & & \mathbf{1} \end{pmatrix}.\quad (25)$$

The upper left corner corresponds to $x < -x_c$, the lower right to $x > x_c$. In practice, it is beneficial to sort the basis such that the central part b^c is in the upper left corner; cf. Appendix A.

Using the unitary transformation (25) leaves the wave function unchanged (see Appendix A). Exploiting the δ structures of the FE-DVR matrix elements Eqs. (19)–(21), very efficient scaling properties of the transformed integrals are obtained. Details of the calculation and the storage scheme for one- and two-electron integrals are given in Appendix B. This approach allows for an accurate treatment of e - e interactions based on the CI expansion including well-chosen single-particle basis functions close to the nuclei as well as an efficient description of wave packets in the continuum through the outer FE-DVR grid. We point out that in contrast to the R -matrix approach, no special attention is needed for assuring physical properties of the wave function across $\pm x_c$ separating the central and outer regions. The communication between the regions is automatically assured by the bridge functions (16), which are constructed from the Lobatto points at $|x| = x_c$ of the underlying FE-DVR basis set.

To demonstrate the smoothness of the wave function at the connection points after the basis transformation and that the density has the correct asymptotic form, we show the single-particle density of the ground state of a model for beryllium (see Sec. IV B) after ITP of the TDSE in Fig. 3, (red) dashed line. No “jumps” or discontinuities can be found, especially not at $\pm x_c$ and the density decays smoothly over the whole simulation grid (note the logarithmic scale of the right axis). The figure confirms that the asymptotic form of the density is

$$n(x) \propto N \exp(-2\kappa|x|),\quad (26)$$

with the parameter κ determined by $I_p = \kappa^2/2$, I_p the first ionization potential, and N a proportionality constant. As a remark, we note that the well-known Brillouin theorem, which states that singly excited determinants do not lower the HF ground-state energy, holds only for the central part $(-x_c, x_c)$ for our scheme. Increasing the grid to $[-x_s, x_s]$ and relaxing the GAS-CI wave function on the whole space lowers the ground-state energy also if only single excitations into the nonrotated part of the basis are included. Illustrative examples are discussed in Secs. IV A 1 and IV B 1.

B. On the choice of single-particle orbitals in the central region

The central region, situated close to the nucleus $(-x_c, x_c)$, is described within a bound-state orbital basis set. In Ref. [32] occupied HF orbitals and pseudo-orbitals $\varphi_i(x) \equiv \varphi_i^{p1}(x)$ constructed from the interaction-free Hamiltonian $\hat{h}_0 = \hat{t} + \hat{v}$ were used, with \hat{v} the Coulomb attraction with the nucleus. The pseudo-orbitals are obtained from the eigenvalue problem

$$(\hat{t} + \hat{v})\varphi_i^{p1}(x) = E_i^{p1}\varphi_i^{p1}(x)\quad (27)$$

and a subsequent orthonormalization onto the occupied HF orbitals. They give an improved description of the virtual, i.e., unoccupied orbitals, compared to the virtual HF orbitals, which tend to be too delocalized (Fig. 4). It turns out, however,

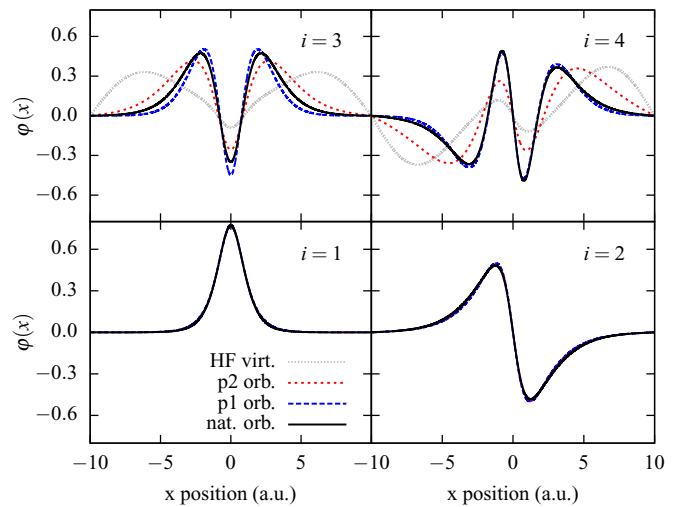


FIG. 4. (Color online) Single-particle orbitals in the central region $[-x_c, x_c]$ for 1D beryllium ($N_{el} = 4$, $x_c = 10$). Comparison of pseudo-orbitals φ_i^{p1} , φ_i^{p2} [cf. Eqs. (27) and (28)] and natural orbitals φ_i^n [Eq. (32)]. The HF virtuals are additionally plotted in gray for comparison. The parameters are the same as in Fig. 3.

that for situations with $N_{el} > 2$, these hydrogenlike orbitals are strongly confined to the nucleus and do not describe valence orbitals well. This defect could possibly explain convergence issues related with photoionization of neon in Ref. [33].

One way around would be the use of an effective charge of the nucleus or a corresponding quantum defect. However, this approach would need proper adjustments according to the considered target. In order to obtain a flexible theory, we propose to use generalized orbitals φ_i^{p2} , which are defined by

$$(\hat{t} + \hat{v} + \hat{v}_H^{N_{el}-2})\varphi_i^{p2}(x) = E_i^{p2}\varphi_i^{p2}(x), \quad (28)$$

with the Hartree potential of the $N_{el} - 2$ system, $\hat{v}_H^{N_{el}-2}$. In coordinate space, it has the form

$$v_H^{N_{el}-2}(x) = \int dx' n^{\text{HF}-2}(x')w(x, x'), \quad (29)$$

with the single-particle density $n^{\text{HF}-2}(x)$ [see also Eq. (33)], which is obtained from a HF iteration with $N_{el} - 2$ electrons. A subsequent orthogonalization of these orbitals to the occupied N_{el} HF orbitals (from a different HF calculation with N_{el} electrons) gives the improved pseudo-orbitals $\varphi_i^{p2}(x)$.

This choice is guided by physical intuition as for systems with one electron in the continuum (relevant for this study), a second electron in the vicinity of the nucleus moves in the effective potential of the $N_{el} - 2$ remaining electrons. We point out that for two-electron systems the choice of orbitals of noninteracting electrons, cf. Eq. (27), coincides with our improved version ($\hat{v}_H^{N_{el}-2} \equiv 0$ for two electrons).

As a third type of orbitals, we construct the natural orbitals, $\varphi_i^n(x)$, which incorporate e - e correlation effects on the single-particle level. They are constructed by first calculating the single-particle density matrix ρ_{pq} within the central region from a highly accurate GASCI (or, if possible, FCI) calculation. The single-particle density matrix is defined as

$$\rho_{pq}^\sigma(t) = \langle \Psi(t) | \hat{c}_{p\sigma}^\dagger \hat{c}_{q\sigma} | \Psi(t) \rangle. \quad (30)$$

For spin-free Hamiltonians, the spatial density matrix is constructed by the spin summation,

$$\rho_{pq}(t) = \sum_\sigma \rho_{pq}^\sigma(t) = \rho_{pq}^\alpha(t) + \rho_{pq}^\beta(t). \quad (31)$$

The natural orbitals are then obtained by a diagonalization of the matrix ρ formed by the elements ρ_{pq} obtained under time-independent field-free conditions,

$$\rho\varphi_i^n(x) = v_i\varphi_i^n(x), \quad (32)$$

where v_i are the natural occupation numbers of the spatial orbitals ($v_i \leq 2$, for HF $v_i = [2, 0]$) and $\varphi_i^n(x)$ are the corresponding natural orbitals. It is well known for electronic ground-state calculations that CI expansions have favorable convergence properties using the basis set formed by natural orbitals [67,76].

The four lowest-lying orbitals ($i = 1, \dots, 4$) of $\varphi_i^{p1}(x)$, $\varphi_i^{p2}(x)$, and $\varphi_i^n(x)$ for a 1D beryllium model (see Sec. IV B) are plotted in Fig. 4 together with the virtual orbitals of the HF method (gray, $i = 3, 4$). For the occupied orbitals ($i = 1, 2$, bottom panels), there exists, by construction, no difference between the HF and the pseudo-orbitals. Only the natural

orbitals show a slight modification. For the convergence of TD-GASCI calculations, however, the virtual orbitals (top panels, $i = 3, 4$) are important because of their strong influence on the construction of excited determinants in the CI expansion.

Whereas the HF virtual orbitals are strongly delocalized, all other types of orbitals remain localized close to the nucleus. As expected, the highest localization is achieved for the hydrogenlike orbitals $\varphi_i^{p1}(x)$ (dashed blue lines). The improved pseudo-orbitals $\varphi_i^{p2}(x)$ show a stronger delocalization (dotted red lines); the natural orbitals are in between (black solid lines). For a discussion of the convergence properties of the TD-GASCI method with respect to the choice of the orbitals, see Sec. IV B. All these orbitals describe a rotated basis for the GASCI expansion and are equivalent regarding completeness (with respect to the underlying FE-DVR basis set). Thus, if results are converged with respect to the e - e correlation, the actual choice of these orbitals is not important. The choice influences, however, the size of the GAS expansion needed for convergence, and therefore, for challenging calculations, the accuracy of the simulation.

C. Observables

In the following, we demonstrate the extraction of several observables of relevance for ionization studies from the GASCI wave function.

The simplest way to extract (single-particle) observables such as densities in real or momentum space from the GASCI wave function is to construct the single-particle density matrix ρ , Eq. (30) or Eq. (31). The single-particle spatial density is given by

$$n(\mathbf{r}, t) = \sum_{p,q} \rho_{pq}(t)\varphi_p^*(\mathbf{r})\varphi_q(\mathbf{r}), \quad (33)$$

which transforms to

$$n(x, t) = \sum_{p,q} \rho_{pq}(t)\varphi_p^*(x)\varphi_q(x) \quad (34)$$

for the case of the 1D partially rotated basis set.

The momentum distribution of one particle can similarly be computed by [46]

$$n(\mathbf{k}, t) = \sum_{p,q} \rho_{pq}(t)\tilde{\varphi}_p^*(\mathbf{k})\tilde{\varphi}_q(\mathbf{k}), \quad (35)$$

with the Fourier transform of the basis functions $\tilde{\varphi}_p(\mathbf{k})$.

For the 1D FE-DVR basis functions, Eqs. (16) and (17), the transformed functions are given for the bridge functions by

$$\tilde{\varphi}_m^i(k) = \frac{\sqrt{w_{n_g-1}^i + w_0^{i+1}}}{\sqrt{2\pi}} \exp(-ikx_{n_g-1}^i) \quad (36)$$

and by

$$\tilde{\varphi}_m^i(k) = \sqrt{\frac{w_m^i}{2\pi}} \exp(-ikx_m^i) \quad (37)$$

for the element functions.

Since we are interested in the momentum or energy distributions of photoelectrons, it is necessary to remove the influence of the potentials of the nuclei. To this end, we assume a large separation of the electronic wave packet from its

binding potential and include only functions outside a certain radius r_{ion} into the calculation of Eq. (35). This corresponds to the projection onto plane waves ignoring the central region. This method is asymptotically exact [77] and applicable since we deal only with single continua in our CAS* schemes. Double continua drastically increase the complexity of the problem [78]. Further, the momentum representation of the transformed orbitals for $|x| < x_c$ does not need to be calculated because typically $r_{\text{ion}} \gg x_c$.

While the total ionization probability can be obtained by integration of the photoelectron spectrum, it is often practical to obtain this quantity by the usage of a complex absorbing potential added to the total Hamiltonian,

$$H^{\text{CAP}}(t) = H(t) - iV_{\text{CAP}}. \quad (38)$$

Throughout, we use a CAP of the form [27]

$$V_{\text{CAP}}(x) = 1 - \cos \left[\frac{\pi(|x| - r_{\text{CAP}})}{2(x_s - r_{\text{CAP}})} \right] \quad (39)$$

for $|x| > r_{\text{CAP}}$ with r_{CAP} the distance from the simulation grid center at which the CAP is turned on. The normalization $\mathcal{N}(t) = \langle \Psi(t) | \Psi(t) \rangle$ of the wave function as function of time provides then a measure of the total ionization probability [5]. For sufficiently long propagation times t_f after the end of the pulse, the continuum part of the wave function has passed r_{CAP} and been absorbed and the total ionization yield is given by

$$\mathcal{P}(t_f) = 1 - \mathcal{N}(t_f). \quad (40)$$

Of course, when using such an approach, it is not possible to discriminate between different ionization channels or single, double, or multiple ionization.

We mention in passing that HHG spectra can be conveniently obtained from the dipole momentum in the acceleration form [27] and the matrix elements of relevance are calculated in analogy to the single-particle potential energy.

D. Summary of simulation method

In total, the TD-GASCI scheme works as follows.

- (1) Set up FE-DVR basis (weights w_i and points x_i) and matrix elements for \hat{t} , \hat{v} , and \hat{w} for $x \in [-x_c, x_c]$.
- (2) Construct (pseudo) orbitals in $[-x_c, x_c]$ by HF calculations or CI ground-state calculations for the case of natural orbitals.
- (3) Construct FE-DVR basis and matrix elements for \hat{t} , \hat{v} , and \hat{w} for $x \in [-x_s, x_s]$.
- (4) Rotate the parts of h_{pq} that belong to the central region and parts of w_{pqrs} ; see Appendix B.
- (5) Construct GASCI initial state for $x \in [-x_s, x_s]$ by ITP.
- (6) Perform TD-GASCI calculation in real time.
- (7) Construct single-particle density matrix $\rho(t)$ and extract observables.

IV. NUMERICAL EXAMPLES

To test and validate the TD-GASCI approach for photoexcitation and ionization phenomena of few-electron atoms, we follow a long tradition in TD calculations and apply the theory to 1D models of atoms [11,12,26–29,73,79–82]. This allows

us to study the convergence properties in direct comparison with accurate simulations of the TDSE.

In our model, the Coulomb binding potential of the nucleus is given by the regularized potential

$$V(x_i) = -\frac{Z}{\sqrt{x_i^2 + s^2}}. \quad (41)$$

The interaction between two electrons at positions x_i and x_j is analogously given by

$$V(x_i, x_j) = \frac{1}{\sqrt{(x_i - x_j)^2 + s^2}}. \quad (42)$$

For all situations considered in this work, we use a softening parameter of $s = 1$. Further, we describe the interaction with the external field in the dipole approximation and use the length gauge, cf. Eqs. (2) and (3), either with a Gaussian half-cycle pulse,

$$F(t) = F_0 \exp \left[-\frac{(t - t_0)^2}{2\sigma^2} \right], \quad (43)$$

or with an electric field with a Gaussian envelope,

$$F(t) = F_0 \exp \left[-\frac{(t - t_0)^2}{2\sigma^2} \right] \cos[\omega(t - t_0) + \varphi_{\text{CEP}}]. \quad (44)$$

The maximum amplitude is denoted by F_0 , the pulse duration by σ , the photon frequency by ω , and the carrier-envelope phase (CEP) by φ_{CEP} .

A. Two-electron model atom (heliumlike)

Let us start with $N_{\text{el}} = 2, Z = 2$, which results in a heliumlike model system for which the TDSE is exactly solvable without further approximations. The exact results are compared with the results of the TD-GASCI approach. We solve the two-particle TDSE by discretizing the two-electron coordinates x_1 and x_2 in the same FE-DVR basis set as for the TD-GASCI using product states (in analogy to Ref. [74]) to exclude any influence from a difference in basis sets. For these brute-force TDSE simulations, no partial rotation of the basis is employed. For the TD-GASCI, we perform the rotation.

1. Ground state

The (small) simulation box ranges from $x_s = \pm 15$ with a rotated basis to described the central region within $x_c = \pm 10$ for the GAS case. The total interval is discretized in $N_g = 30$ elements, each of which has $n_g = 8$ DVR functions. This gives a total of 209 FE-DVR functions, of which 139 are rotated to pseudo (or natural) orbitals. The relevant GAS partitions for this two-electron system are sketched in Fig. 5 together with a description of the nomenclature; see also Sec. II B.

The ground-state energies (GSEs) for different GASCI approximations obtained by ITP are summarized in Table I. As expected, the HF approximation GSE is larger than the exact TDSE value. We further note that the HF results are mostly converged with respect to the central region (“center” vs “all”) and only the last digit differs. By applying the simplest GAS approximations (SAE and CIS), we retain the well-known Brillouin theorem by recovering the HF energy of the whole simulation range $[-x_s, x_s]$ exactly.

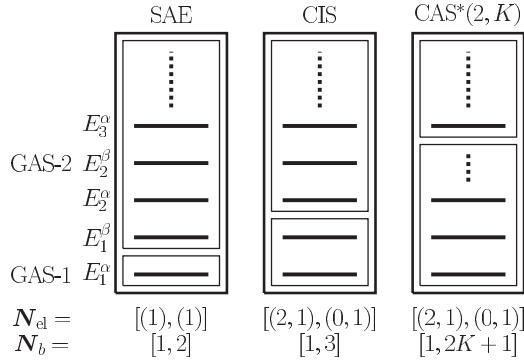


FIG. 5. GAS partitions for the two-electron model. The acronyms of the different approximations are SAE, single-active electron; CIS, configuration-interaction singles; CAS*(2, K), complete active space with a CAS including K spatial orbitals and single excitations outside. See Fig. 1 and Sec. II B for notations.

Adding more pseudo-orbitals to the lowest GAS, resulting in a CAS with double excitations up to including $2K$ spin orbitals and single excitations above this level [CAS*(2, K)], lowers the GSE. Convergence is achieved for the case CAS*(2, 27) with 10557 configurations in the expansion. This value for the GSE is limited by the choice of x_c . By including also the nonrotated part for double excitations, we recover the TDSE limit exactly up to machine precision (FCI) with 43 681 configurations. We note that with about 10 times less configurations an excellent approximation for the GSE is achieved.

2. Ionization yields and photoelectron spectra

As pointed out in Ref. [32], the TD-RASCI approach allows for an accurate calculation of photoionization cross sections including the relevant multiple-excited states. A systematic investigation of the influence of the partially rotated basis was, however, not carried out. To test the method against TDSE simulations, we prepare the 1D heliumlike model in its ground state and shine a long Gaussian-shaped pulse [Eq. (44)] of length $\sigma = 100$ and strength $F_0 = 0.001$ centered at time

TABLE I. Ground-state energy as function of GAS for the two-electron heliumlike model. “Center” refers to a HF calculation for $|x| \leq x_c$ and “all” for $|x| \leq x_s$. The total number of spin orbitals is $2N_b = 2 \times 209$. See Fig. 5 and Sec. II B for a definition of the GAS spaces and the notations.

Method	N_{el}	N_b	n_{conf}	Energy [a.u.]
HF center			1	-2.224 209 54
HF all			1	-2.224 209 55
SAE	$[(1), (1)]$	$[1, 2]$	209	-2.224 209 55
CIS	$[(2), (1), (0, 1)]$	$[1, 3]$	417	-2.224 209 55
CAS*(2, 2)	$[(2), (1), (0, 1)]$	$[1, 5]$	832	-2.236 176 24
CAS*(2, 3)	$[(2), (1), (0, 1)]$	$[1, 7]$	1245	-2.237 477 55
CAS*(2, 11)	$[(2), (1), (0, 1)]$	$[1, 23]$	4477	-2.238 202 92
CAS*(2, 27)	$[(2), (1), (0, 1)]$	$[1, 55]$	10 557	-2.238 257 72
FCI	$[(2)]$	$[1]$	43 681	-2.238 257 82
TDSE				-2.238 257 82

$t_0 = 400$ and with $\varphi_{CEP} = 0$. Note that the electric field strength of the rather long pulse is clearly in the perturbative regime to avoid saturation of the ionization yield also in the case of resonant excitation. We propagate to a final time of $t_f = 4000$ to allow for a reasonable decay of all excited resonances.

To facilitate a large number of calculations for different photon frequencies, we choose a rather small system size of $x_s = \pm 40$ with the atom centered at $x = 0$. The central region is connected at $x_c = \pm 10$ and a total FE-DVR basis set of 40 elements with seven DVR functions has been used. The total ionization yield $\mathcal{P}(t_f, \omega)$ is extracted from Eq. (40) with a CAP starting at $r_{CAP} = 20$ in Eq. (39).

In addition to the photoionization with a rather long pulse, we, in a different calculation, excite the system with a δ -like [$\sigma = 0.1, t_0 = 1, F_0 = 0.001$ in Eq. (43)] dipole kick and record the dipole response $\langle x(t) \rangle$ over a long time ($t_f = 3000$). A Fourier transform with respect to the time,

$$S(\omega) = |\mathcal{F}\{x(t)\}|^2, \quad (45)$$

gives the dipole excitation spectrum [82]. For better visibility of the positions of the resonances, we apply a Blackman window [83] to the data before applying the discrete Fourier transform.

The ionization yields $\mathcal{P}(t_f, \omega)$ as a function of the photon energy ω for different GAS approximations and the corresponding TDSE result are shown in Fig. 6 together with the dipole spectrum $S(\omega)$ from a TDSE calculation (gray line). The resulting peaks in Fig. 6(a) can be classified into two groups: (i) single excitations up to $\omega \approx 0.9$ and (ii) double excitations above $\omega \approx 1.2$. Group (i) corresponds to the excitations of one electron into higher states, where the other electron is still bound in its ground-state orbital. These are labeled by $1eno$, where e (o) denotes an orbital that is even (odd) under the parity operation. This series converges to the first ionization threshold $I_p^{(1)}$ for $n \rightarrow \infty$ and is visible in all GAS approximations, ranging from SAE to the fully converged TDSE result at approximately the correct position. We note, however, that the SAE approximation (lower dashed orange line labeled “SAE”) underestimates the yield by about a factor of 2, whereas CIS overestimates the yield (dashed blue line).

Figure 6(b) shows a magnification of the region relevant for single excitations ($1eno$) and compares the results obtained using different types of orbitals in the central region. We find that pseudo-orbitals $\varphi^{p1}(x)$ (dashed blue lines) and natural orbitals $\varphi^n(x)$ (dash-dotted red lines) describe the single excitations well and perfect agreement with the TDSE (black solid line) is achieved for CAS*(2, 6), where the GAS consists of an active space of six spatial orbitals and single excitations above, and practically no difference is visible. Further, for the smaller CAS*(2, 2) calculation with nonconverged $e-e$ correlation contributions, the differences between pseudo- and natural orbitals are only marginal (dotted blue vs dash-dotted red lines).

A slightly different picture arises for the two-electron resonances (ii). A magnification of the $2one$ series, i.e., the simultaneous excitation of one electron into the first excited state and of the other electron to all possible higher states, is shown in Fig. 6(c). These resonances are absent for the SAE and CIS approximations and appear only if double excitations

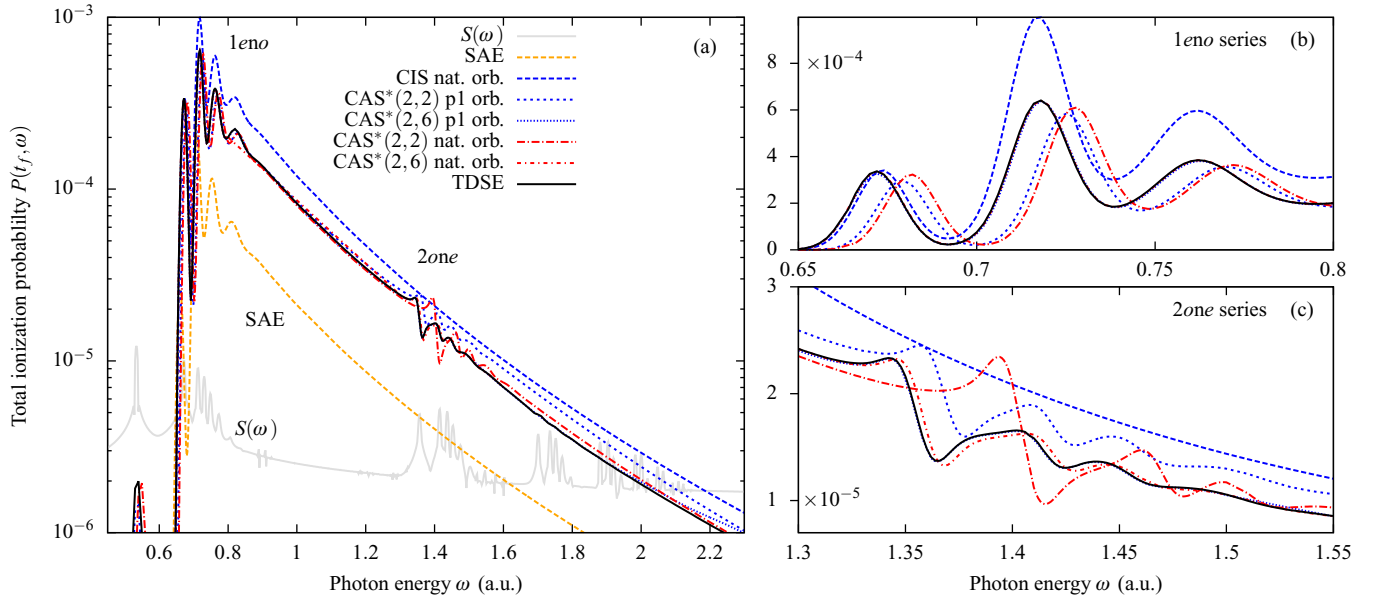


FIG. 6. (Color online) Ionization probability $\mathcal{P}(t_f = 4000, \omega)$, cf. Eq. (40), of the heliumlike model for different GAS approximations as a function of the photon energy for a fixed pulse duration. The results for pseudo-orbitals φ^{p1} , Eq. (27), and natural orbitals φ^n , Eq. (32), in the rotated basis are compared. The left panel (a) shows the whole range of frequencies on a logarithmic scale and the right panels magnifications of the one-electron excitations (1eno, b) and the first two-electron resonances (2one, c) on a linear scale. The dipole-excitation spectrum $S(\omega)$ [cf. Eq. (45)] for an infinitesimally short pulse from a fully correlated TDSE simulation is drawn in gray to help identify the positions of the excited states. The field parameters are $F_0 = 0.001, \sigma = 100, t_0 = 400, \varphi_{\text{CEP}} = 0$ in Eq. (44).

are included into the GAS. Again, good agreement with the TDSE is achieved for large CAS*(2,6); however, it turns out that there is a difference in the convergence behavior for natural and pseudo-orbitals for small CAS*(2,2), i.e., not fully correlated calculations. Where the natural orbitals $\varphi_i^n(x)$ (dash-dotted red lines) have problems in describing the correct energy position of the resonances, the pseudo-orbitals $\varphi_i^{p1}(x)$ overestimate the overall ionization yield (dotted blue lines) but predict better excitation energies.

This behavior is even more pronounced for calculations of the photoelectron spectra, which are shown in Fig. 7. The spectra were obtained with the method described in Sec. III C (see also Ref. [46]), and a radius of $r_{\text{ion}} = 20$ was used for ionization.

Calculations were performed for $F_0 = 0.01, \sigma = 5, \varphi_{\text{CEP}} = 0$, and $\omega = 2.1$ in Eq. (44), which results in a rather broad excitation bandwidth. The results for pseudo-orbitals are shown in Fig. 7(a) and for natural orbitals in Fig. 7(b), together with the TDSE result (black line). The insets show a magnification of the correlation satellites (“shake-up”) at lower photoelectron energy, which are nearly invisible in the total spectra. In these processes, the photon energy is shared between the photoelectron and a second, still bound electron. The result is a slower photoelectron, which gives the correlation peak in the energy distribution, and an ion in an excited state.

The main peak at an energy of 1.3 is well described in position and shape by both types of orbitals and the different CAS* approximations considered. For small active spaces as in CAS*(2,2) (dashed blue line), this peak is drastically underestimated for both types of orbitals. An even more pronounced influence of the CI truncation can be observed

in the satellites below an energy of about 0.8 (insets). Note that the case of CAS*(2,2) has been scaled by a factor of 0.1 in the insets.

For a limited active space the choice of the orbitals becomes vital and natural orbitals describe the shape of the peak and its magnitude better. Especially the excitations for CAS*(2,6) into higher orbitals (lower resulting photoelectron energy) is significantly closer to the TDSE result than the CAS*(2,2) results. Since both choices of orbitals represent rotations in the space of virtual (i.e., unoccupied) HF orbitals and both form a complete single-particle basis, the results converge toward the TDSE solutions in the limit of a large active space [red dotted lines for CAS*(2,11)].

B. Four-electron model atom (berylliumlike)

We now consider the more complex model with $N_{\text{el}} = Z = 4$ in Eq. (41), which results in a berylliumlike 1D model. It can be solved exactly only for very special situations, e.g., with TD-FCI or TDSE simulations for very small simulation boxes and single-particle basis sets.

The relevant GAS partitions are shown in Fig. 8. In contrast to helium, the four electrons occupy the two lowest-lying spatial orbitals, which we refer to as “core” (c) and “valence” (v) orbitals in the following. Thus, we can define SAE approximations for the core and the valence orbitals, respectively. In analogy, we can define CIS-like approximations and active spaces with two [CAS*(2,K)] or all four [CAS*(4,K)] electrons being active. For CAS*(2,K), the inner-shell electrons are frozen and for the outer-shell electrons, double excitations up to spatial orbital K are included. For CAS*(4,K), analogously, all electrons can

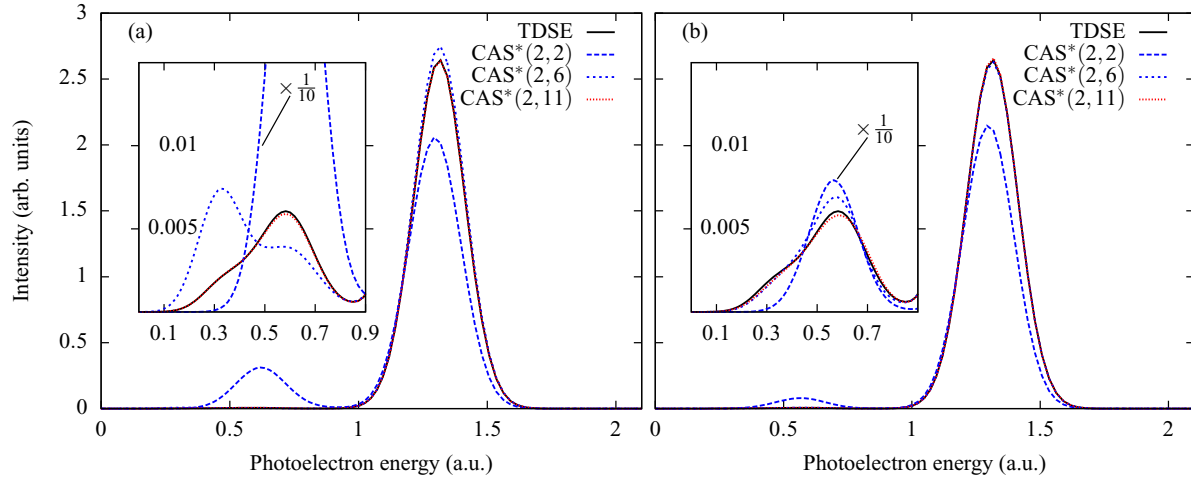


FIG. 7. (Color online) Photoelectron spectra of the 1D heliumlike model for a short pulse [Eq. (44)] with $\sigma = 5$, $F_0 = 0.01$, $\varphi_{\text{CEP}} = 0$ and a photon energy of $\omega = 2.1$ using (a) pseudo-orbitals $\varphi_i^{p1}(x)$ and (b) natural orbitals $\varphi_i^n(x)$. The CAS*(2,2) results are scaled by a factor of 1/10 in the insets.

occupy the K spatial orbitals, which also includes fourfold excitations. For both situations, single excitations out of the CAS are included.

1. Ground state

The GSEs as a function of the GAS partition are collected in Table II for different pseudo-orbitals $\varphi_i^{p1}(x)$ and $\varphi_i^{p2}(x)$ [cf. Eqs. (27) and (28)] and a multiconfiguration time-dependent Hartree-Fock (MCTDHF) calculation [13]. The parameters for

the simulation box (x_s and x_c) and the FE-DVR basis are the same as for helium; see Sec. IV.A.

As expected, the HF GSE is above the fully correlated reference result. The two SAE approximations give an impression of the influence of the choice of x_c . Where an active core orbital (SAE-c) gives exactly the same GSE as the HF result up to numerical precision (which is a manifestation of the Brillouin theorem), an active valence orbital (SAE-v) lowers the GSE. This can be understood by the larger spatial extension of the valence orbital in comparison to the core orbital. The former exceeds the central region, for which the HF calculation was performed, while the strongly localized core orbital is completely captured within the region $\pm x_c$. During the ITP of the TD-GASCI equations, the initial wave function constructed from the valence orbital is allowed to relax on the increased grid. This results in a lower GSE, even if only single excitations are included. The error in the GSE due to the choice of x_c is on the order of 10^{-5} for these parameters. A similar observation

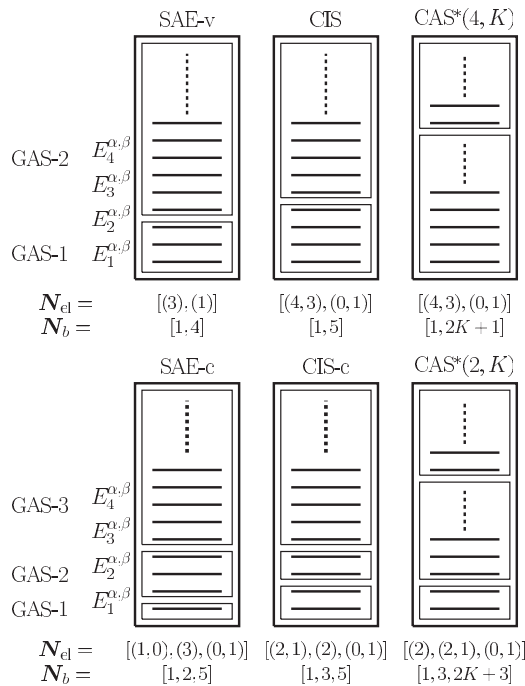


FIG. 8. Schematics of the GASs for the four-electron beryllium-like model. The label v (c) refers to an active valence (core) orbital. CAS*(2, K) and CAS*(4, K) are active spaces with two and four electrons, respectively, with single excitations out of the CAS. The case CIS-v equals CAS*(2,1). See also Fig. 2 and Sec. II B.

TABLE II. The same as Table I but for beryllium. The energies E_0^1 and E_0^2 correspond to the pseudo-orbitals φ_i^{p1} and φ_i^{p2} , respectively.

Approximation	n_{conf}	E_0^1	E_0^2
HF ($-x_c, x_c$)	1	-6.739 419 16	
SAE-v	208	-6.739 434 39	-6.739 434 39
SAE-c	208	-6.739 419 16	-6.739 419 16
CIS-v	415	-6.739 449 60	-6.739 449 60
CIS-c	415	-6.739 419 16	-6.739 419 16
CIS	829	-6.739 449 61	-6.739 449 61
CAS*(2,2)	828	-6.770 020 39	-6.769 608 58
CAS*(2,3)	1239	-6.773 753 20	-6.772 660 39
CAS*(2,21)	8295	-6.774 867 86	-6.774 867 57
CAS*(2,41)	15375	-6.774 868 25	-6.774 868 25
CAS*(4,3)	3717	-6.777 932 24	-6.774 281 36
CAS*(4,4)	9876	-6.783 253 75	-6.779 407 15
CAS*(4,10)	181125	-6.784 912 05	-6.784 395 62
MCTDHF [13]	10^4		-6.7851

^aIn this method, the orbitals and thus the configurations are TD.

can be made for the CIS-v and -c approximations with an active valence or core orbital. The lowest energy for CIS is obtained when all four electrons are allowed to relax on the entire simulation grid.

For the GAS partitions with only single excitations, the choice of the virtual space, i.e., the rotated orbitals within $(-x_c, x_c)$ is unimportant because all orbitals are included on the same level. Therefore, both types of pseudo-orbitals give exactly the same value for the GSE. The account for correlations, either by two or by four active electrons, changes this picture. Two limits of e - e correlations can be defined: (i) with frozen core [CAS*(2, K)] and (ii) with all electrons active [CAS*(4, K)]. For (i), the lowest energy is reached for about $K = 41$, where both types of pseudo-orbitals converge to the same result and an increase of the active space does not change the GSE. For smaller active spaces, however, we observe a better, i.e., lower, ground state using the hydrogenlike pseudo-orbitals $\varphi^{p_i}(x)$. This effect is seen most clearly for the first correction to the CIS result, CAS*(2,2). For (ii) with four active electrons, the number of configurations increases dramatically due to the exponential scaling [cf. Eq. (10)], and the GSE is lowered significantly. Again, better results are obtained with the pseudo-orbitals of type $\varphi^{p_i}(x)$.

Finally, we note that our method with 181125 configurations, CAS*(4,10), does not reach completely the fully correlated GSE of the MCTDHF calculation, where in addition to the expansion coefficients of the wave function also the single-particle orbitals are allowed to relax. In contrast to TD-GASCI, the MCTDHF method considers a FCI approach with TD orbitals. Thus, for advancing in time, in addition to the expansion coefficients $C_I(t)$, like in TD-GASCI, also the orbitals need to be propagated. This results in a nonlinear, numerically complex and demanding scheme of which the properties for TD calculations in the context of photoionization remain to be fully explored. Further, MCTDHF calculations are feasible for $N_{el} \lesssim 10$ with highly optimized codes. Currently, progress towards larger systems is made using a combination of restricted-active spaces and TD orbitals in the TD-RASSCF theory [27–29].

2. Excitation spectra

We now turn our attention to the TD properties of TD-GASCI by considering the dipole excitation spectrum $S(\omega)$ [cf. Eq. (45)] of the 1D four-electron berylliumlike model. The spectra are calculated by exciting the system with a small δ kick of the ground-state wave function and the Fourier transform of the TD dipole $\langle x(t) \rangle$; cf. Sec. IV A 2 for method and parameters.

The results for various GAS partitions are compiled in Fig. 9. We define ionization potentials, I_p^v and I_p^c , for the valence and the core orbitals, respectively. In first approximation, they are according to Koopman's theorem given by the corresponding energy of the occupied HF orbitals. For the SAE approximations, the ionization potentials are recovered in the dipole spectrum by a series of excitations, which converge toward $I_p^{v/c}$ (dashed vertical lines in Fig. 9). A similar behavior is found for the CIS approximation of the valence and the core electrons. For the complete CIS calculation, both series are resolved; i.e., excitation from the core and the valence orbital

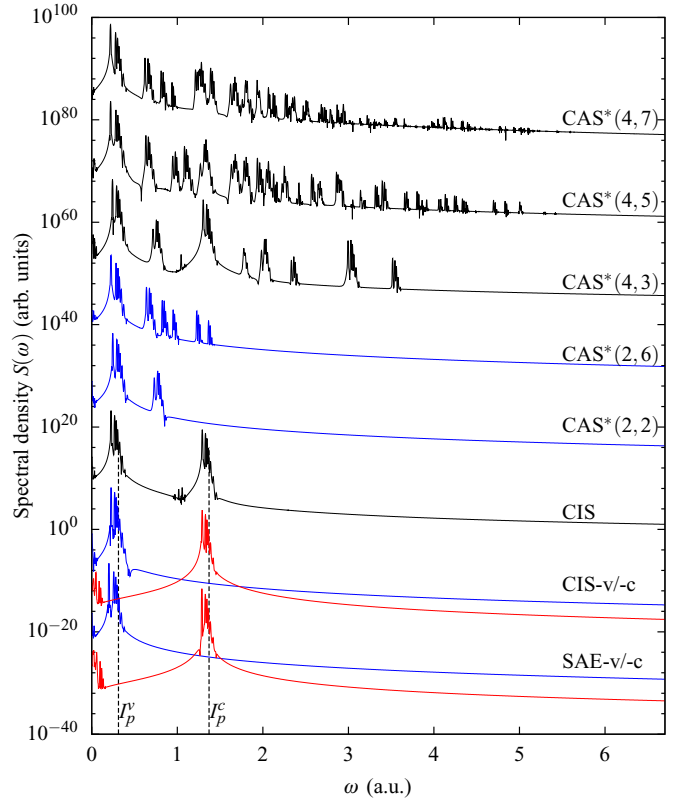


FIG. 9. (Color online) Dipole excitation spectrum $S(\omega)$ [cf. Eq. (45)] of the 1D four-electron berylliumlike model for an excitation of $\sigma = 0.1$, $t_0 = 1$, $F_0 = 0.001$ [Eq. (43)] in different GAS approximations; shown is the total energy range from the GSE to full fourfold ionization ($I_p^4 = -E_0$). The first ionization potentials for ionization from the valence orbital, I_p^v , and core orbital, I_p^c , are indicated by dashed vertical lines. The labels “v” and “c” refer to the valence and core orbitals, respectively. Red lines (higher energy, limited by I_p^c) correspond to core electrons only; blue is for the valence shell (lower energy, I_p^v).

is possible, but not two electrons simultaneously, which results in structureless continua between I_p^v and I_p^c and above I_p^c .

In these regions, multielectron resonances appear as a consequence of the allowance for multiple excitations in the GAS partition. For frozen-core calculations, CAS*(2, K), additional peaks arise above I_p^v due to the simultaneous excitation of two valence electrons into a doubly excited state and its subsequent decay with one electron in the continuum. The spectra become much more complex if all four electrons are active, CAS*(4, K). For these, doubly, triply, and quadruply excited states are accessible and appear as multiple-excited resonances in the dipole spectrum. These excitations converge towards an energy where all four electrons are liberated ($I_p^{(4)} = -E_0 \simeq 6.78$). Thus, besides its computational advantages and systematic approach to e - e correlation effects, TD-GASCI allows additionally for a clear interpretation of excitation spectra in terms of systematic adding of configurations to the expansion (13).

3. Orbital influence on TD-GASCI convergence

In Sec. IV B 1, we discussed the influence of the type of the pseudo-orbitals on the GSE of the system and found that

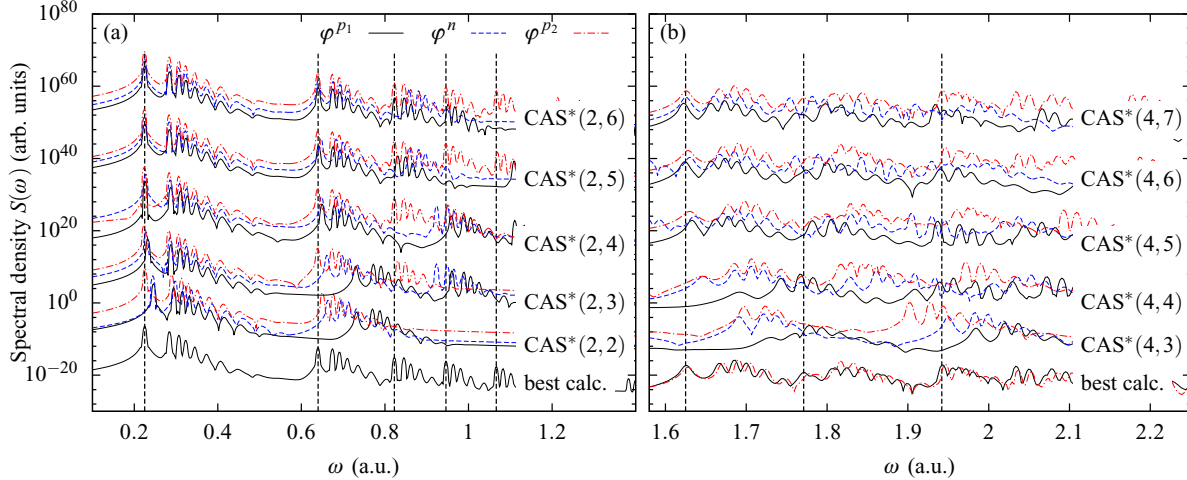


FIG. 10. (Color online) Parts of the dipole excitation spectrum $S(\omega)$ of the four-electron berylliumlike model for different GAS approximations and orbital basis sets in the central region. (a) Fixed core; (b) all electrons are active. Dashed vertical lines are guides to the eye for reference to the best [CAS*(2,11) for (a) and CAS*(4,7) for (b)] approximation (bottom line). The individual lines are vertically shifted for better visibility. The full spectrum and parameters are given in Fig. 9.

$\varphi^{p1}(x)$ [Eq. (27)] outperform $\varphi^{p2}(x)$ [Eq. (28)] for ground-state calculations. In Fig. 10, the dipole spectra $S(\omega)$ for different CAS* approximations and the three types of orbitals, $\varphi^{p1}(x)$, $\varphi^{p2}(x)$, and $\varphi^n(x)$ [Eq. (32)], are shown. Figure 10(a) shows GAS approximations with two active electrons in the spectral region below the excitation energy of core electrons (cf. Fig. 9) in which the energies of the single- and double excitations of the valence electrons are located. The lowest black line shows the converged result obtained by a CAS*(2,11) calculation and dashed vertical lines the lower threshold energy of each series as a guide to the eye.

The first series corresponds to the one-electron excitations and is well represented in all CAS* approximations for each type of orbitals. We notice, however, that the $\varphi^{p2}(x)$ pseudo-orbitals of type 2 (dash-dotted red lines) have better convergence properties and reproduce the correct position in energy already in the lowest CAS* approximation. For the two-electron resonances the influence of the orbital choice becomes more pronounced. For all considered approximations, the pseudo-orbitals $\varphi^{p2}(x)$ perform better, and the higher-lying series are closer to the converged result. A similar statement can be made for natural orbitals with respect to the first double-excitation series; however, higher series are more off the correct result. The worst result is obtained with the pseudo-orbitals of type $\varphi_i^{p1}(x)$, which are only able to reproduce resonances at the correct positions if the active space is much larger than that of the other orbitals.

The case of four active electrons above I_p^c is shown in panel (b), where higher excited resonances appear in the spectrum. Again, the best result for CAS*(4,7) is shown in the bottom. Here, due to the complex spectrum, a clear classification of the orbitals is difficult. However, we find that also for this case the improved orbitals $\varphi^{p2}(x)$ perform well and predict excitations at the correct positions. For the calculation of fourfold excitations, the choice of the orbitals is less important and active spaces chosen too small result in wrong excitation energies for all orbitals, as well as the improved ones. However, we note that $\varphi^{p2}(x)$ are especially

designed for double excitations of the valence electrons by considering the $N_{\text{el}} - 2$ -electron problem for the calculation of an effective potential. Generalizations of this scheme to orbitals calculated from $N_{\text{el}} - 3$ or $N_{\text{el}} - 4$ potentials in order to describe the removal of two or more electrons in combination with excited states of the ion are difficult. The main problem is that such generalized single-particle orbitals need to describe the removal of a single electron accurately in addition to the above-mentioned effects.

In total, the pseudo-orbitals of type $\varphi^{p2}(x)$ outperform natural $\varphi^n(x)$ and type $\varphi^{p1}(x)$ pseudo-orbitals in TD excitation scenarios if two-electron excitations are considered. We expect this favorable property of the φ^{p2} -type orbitals to improve 3D calculations for real atoms and molecules as well.

C. Molecular model systems

To demonstrate the generality of the TD-GASCI approach, we present in the following a study of the GSE and the nonperturbative dynamics of a diatomic molecule in a strong field.

Consider, for each electron, the 1D diatomic potential consisting of two atomic species,

$$V(x, R) = -\frac{Z_1}{\sqrt{(x - \frac{R}{2})^2 + 1}} - \frac{Z_2}{\sqrt{(x + \frac{R}{2})^2 + 1}}, \quad (46)$$

with x the electron coordinate, R the internuclear distance, and Z_i ($i = 1, 2$) the nuclear charges. A two-electron hydrogenlike molecule is then defined by $Z_1 = Z_2 = 1$ and a four-electron lithium-hydride equivalent by $Z_1 = 3$ and $Z_2 = 1$. Such models are well established in the literature, e.g., [11, 12, 26, 73, 84]. We point out that for $x_c \gg R$, the choice of the grid reference, i.e., center of mass, center of charge, or the geometric center of the molecule, does not influence the calculations. For the calculation of absolute values for dipoles, however, this reference has to be taken into account.

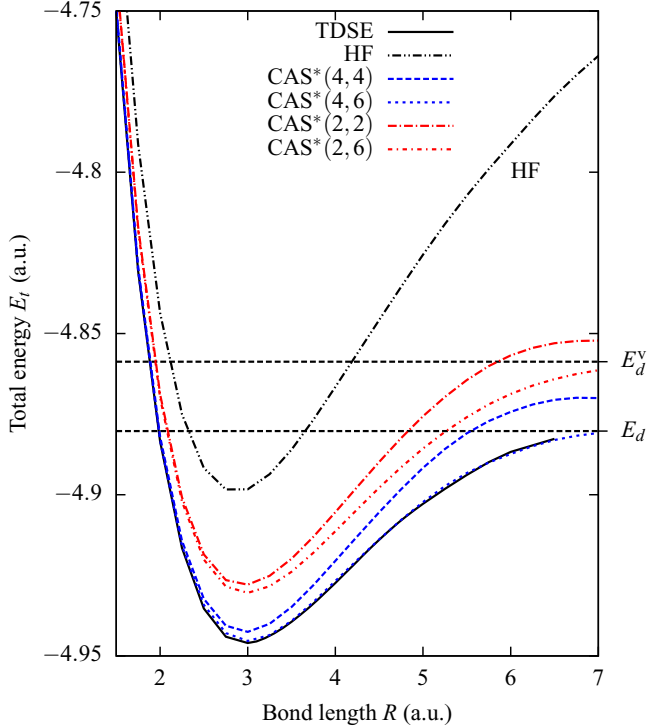


FIG. 11. (Color online) Total energy of the 1D four-electron LiH-like model. The dissociation limit is indicated by dashed lines for fully relaxed Li (E_d) and for Li with fixed core (E_d^v). See text for details. Dot-dashed and dot-long-dashed red lines converging to E_d^v are for two active [CAS*(2,.)] electrons, blue lines converging to E_d for all four being active [CAS*(4,.)]. The TDSE result (full black line) is for a smaller FE-DVR basis set [11].

1. Ground-state properties

The total energy of the system, corresponding to the Born-Oppenheimer energy surface, is calculated by

$$E_t = E_{\text{el}} + \frac{Z_1 Z_2}{\sqrt{R^2 + 1}}, \quad (47)$$

where E_{el} denotes the total electronic GSE. We note that, in contrast to Ref. [11], the internuclear repulsion is also regularized. This is necessary to treat both interactions on a similar footing and obtain a correct convergence towards the dissociation limit, E_d .

The total energy of the 1D four-electron LiH-like model as function of the internuclear distance R is shown in Fig. 11. Parameters for the calculation are $x_s = \pm 50$ and $x_c = \pm 10$. The box is discretized by 50 elements, of which each contains eight DVR functions. The GAS nomenclature is as for the four-electron atomic model; see Fig. 8. For this prototype four-electron model molecule, reference results are available in the literature [11]. As expected, the closed-shell restricted HF code does not predict the correct dissociation threshold E_d for Li and H in their corresponding ground state. Similar behavior is observed for the SAE- v and CIS- (v) approximations in this basis (not shown in the figure). Including more configurations in the central region, however, repairs this behavior and the potential energy curve converges quickly (for only four

additional spatial orbitals in the active space) towards the four-particle reference TDSE results.

Two different dissociation thresholds, i.e., the GSE of the fragments at infinite internuclear distance, are indicated in Fig. 11: E_d corresponds to a FCI calculation of Li ($|Z| = N_{\text{el}} = 3$) and E_d^v to a calculation, where the $1s$ level in Li was fixed and only the unpaired valence electron was allowed to relax. For GAS calculations with fixed inner-shell electrons and only two active, CAS*(2, K), the dissociation limit of the LiH molecule corresponds to the energy E_d^v and is correctly reproduced by including about six spatial orbitals in the active space.

2. Strong-field ionization

In this section, we illustrate the potential of the TD-GASCI method by studying the influence of e - e correlation on the preferred direction of electron ejection with respect to the external field and molecular orientation in the heteronuclear polar diatomic LiH-like 1D model molecule subject to strong-field ionization at 800 nm. There is currently a strong interest in the elucidation of this question. For example, in the OCS molecule, experiments with circularly polarized light and theory show that ionization occurs most readily from the O end, i.e., when the field points towards the S end [85–87]. For linearly polarized light, on the other hand, one experiment reports most ionization from the S end [88], while another most perpendicular to the molecular axis [89]. For the CO molecule, as another example, strong-field ionization experiments performed in the tunneling regime report that ionization occurs most readily when the external field has a component pointing from the C to the O end, and the electron leaves from the C end [90–92].

This is in contrast with the results from application [87,93] of SAE approximation tunneling theory [84], which predicts that ionization is most likely when the field points from the O to the C end. Recently, many-electron effects expressed in terms of dynamic core polarization as accounted for at the TDHF mean-field level of theory were shown to improve the agreement between experiment and theory [94]. Also, in the future, many-electron effects may be addressed by application of many-electron tunneling theory [95]. Clearly, the TD-GASCI approach is particularly well suited for an investigation of many-electron effects on the preferred electron ejection direction since e - e correlation can be added in a controllable manner by suitably extending the active space.

We begin the study by preparing the LiH-model molecule in its electronic ground state at the equilibrium distance of $R = 3$; cf. Sec. IV C 1. A short Gaussian-shaped single-cycle [Eq. (44)] 800-nm pulse ($\omega = 0.57$) of duration $\sigma = 30$ with electrical field amplitudes of (i) $F_0 = 0.025$ and (ii) $F_0 = 0.05$ excites the system. For a fixed orientation of the molecule, the peak of the field can be oriented towards the nucleus of either Li or H, depending on on the CEP, φ_{CEP} . In Fig. 12 the considered cases $\varphi_{\text{CEP}} = 0$ and $\varphi_{\text{CEP}} = \pi$ are sketched.

To calculate the total ionization yield $\mathcal{P}(t_f)$, cf. Eq. (40), for a given φ_{CEP} , a CAP [Eq. (39)], which removes liberated electrons from the simulation box of size $|x_s| = 200$, is placed at a distance of $r_{\text{CAP}} = 100$ from the center of the grid. We

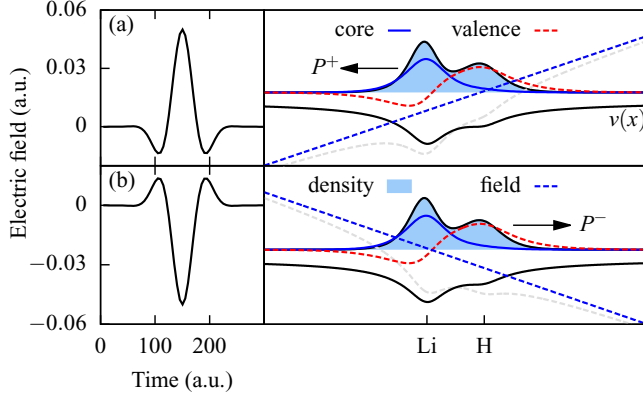


FIG. 12. (Color online) Sketch of the scenarios considered with the 1D four-electron LiH-like model molecule under strong-field ionization. The electric field $F(t)$ is shown in the left part for (a) $\varphi_{\text{CEP}} = 0$ and (b) $\varphi_{\text{CEP}} = \pi$. The two doubly occupied core and valence HF orbitals are plotted along with the single-particle initial density and potential. For better visibility of the densities, the dipole potential (diagonal dashed lines) at the time of maximum electrical field is magnified in the figure.

checked carefully for the influence of the CAP parameters on the observable and compared to simulations with very large box sizes without a CAP (cf. Fig. 13) and no significant change of the results presented were observed. Results are shown for pseudo-orbitals of type 1 with $|x_c| = 10$. We redid part of the calculations with type 2 orbitals and obtained similar results for the limit of large CAS* spaces.

The equations of motion are propagated to a final time of $t_f = 15\,000$, which allows for slow electrons to reach the absorber and thus record the total ionization yields, \mathcal{P}^\pm , for positive (+) and negative (−) peak electric field amplitudes. We define the ratio

$$\eta = \frac{\mathcal{P}^-}{\mathcal{P}^+}, \quad (48)$$

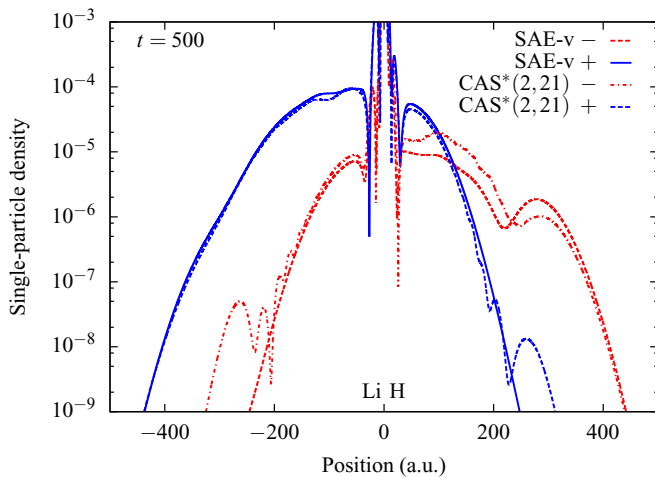


FIG. 13. (Color online) Single-particle density $n(x)$ [cf. Eq. (34)] of the 1D four-electron LiH-like molecule exposed to single-cycle pulses (i) after a propagation of $t = 500$.

TABLE III. Parameter η of Eq. (48) for single-cycle ionization of the 1D four-electron LiH-like model molecule for peak electrical field strength (i) $F_0 = 0.025$, (ii) $F_0 = 0.05$. For $\eta < 1$ ($\eta > 1$) ionization is more likely when F_0 points in the direction of Li (H). The left-hand side of the table shows GAS results with active valence and fixed core electrons. The right-hand side of the table shows GAS results where all four electrons are active.

GAS	(i)	(ii)	GAS	(i)	(ii)
SAE-v	0.12	0.27	CIS	0.16	0.31
CIS-v	0.16	0.31	CAS*(4,3)	0.30	0.48
CAS*(2,2)	0.29	0.44	CAS*(4,4)	0.24	0.43
CAS*(2,3)	0.22	0.39	CAS*(4,5)	0.22	0.44
CAS*(2,6)	0.23	0.42			
CAS*(2,11)	0.23	0.42			
CAS*(2,21)	0.23	0.42			

which is smaller (larger) than 1 if it is more (less) likely to ionize for the situation in the top panels in Fig. 12 than in the bottom panels. Furthermore, $\eta = 1$ is obtained in the case of equal ionization probability $\mathcal{P}^+ = \mathcal{P}^-$, which is the case for the homonuclear molecules.

The results for η for different GAS approximations ranging from SAE to including up to 21 orbitals in the active space are given in Table III for both electrical field strengths (i) and (ii). Let us first discuss LiH at the lower intensity (i). For all approximations, ionization is favored when $\varphi_{\text{CEP}} = 0$ and $F(t)$ is positive at its maximum. In this case the electron is liberated in the direction of Li [Fig. 12(a)]. This preference for ionization in this relative geometry is largest for the simplest possible and most commonly used SAE approximation. Correlation effects shift this result toward more symmetry in the ionization dynamics by a factor of approximately two. We further note that an active core orbital [CAS*(4, K), right in Table III] does not strongly impact the results since the active core and fixed core [CAS*(2, K), left in Table III] results are quite similar.

By increasing the laser intensity, case (ii), a corresponding behavior is observed, but with a much less pronounced favored direction of ionization (η is larger). This can be explained by the drastically increased total ionization yield compared to (i) due to a field strength $|F_0| = 0.05$ which is above the over-the-barrier field strength of about $I_p^2/4 = 0.034$ for the valence orbital. For that case, any preference of direction of the electron emission is suppressed.

To learn more about the effect of $e-e$ correlation, we additionally performed calculations on a large numerical grid and calculated the single-particle densities for the case of SAE and the converged result of two active electrons, CAS*(2,21), for the lower laser intensity (i). The results are given in Fig. 13 for both CEPs of the field after the field is turned off ($t = 500$). In the logarithmically scaled density plot, it becomes apparent for the SAE approximation that ionization is favored if the field points toward the H atom (“+”, blue). Correlation has nearly no effect on the single-particle density in this direction but changes the density emitted in the opposite direction (“−”, red). Here the small fraction for the SAE case is drastically enhanced for the correlated case (dashed line), which, in turn, results in an increase of the asymmetry parameter η .

V. CONCLUSIONS AND OUTLOOK

In this paper, we described and applied the time-dependent generalized-active-space configuration-interaction scheme to solve the multiparticle TDSE. The key for the efficient use of TD-GASCI for photoionization of atoms and molecules involving continua is the use of a partially rotated basis set with HF and pseudo-orbitals to describe the confined bound-state orbitals. Using 1D heliumlike and berylliumlike models, we gave a detailed analysis of the convergence behavior with respect to the considered orbitals used for the rotation and found that improved pseudo-orbitals based on the $N_{el} - 2$ HF problem are well suited for TD calculations involving single-electron continua.

We applied the TD-GASCI method to the strong-field ionization of the 1D four-electron LiH-like model and found a strong dependence of the observed ionization yield as a function of the orientation of the molecule with respect to the peak electric field direction and in particular on the included level of e - e correlation. The e - e interaction increases the ionization yield in the direction of H. We expect these effects to play a role also in 3D systems.

Although our presented results are for 1D systems, the method is completely general and can be applied “as is” in arbitrary coordinates. The restriction in dimensionality in this work allowed for a detailed validation of the method through comparison with fully converged correlated calculations based on the TDSE. The usability of the similar TD-RASCI approach to single-photon absorption in beryllium and neon in a spherical basis set was demonstrated in [32,33], with the focus on the comparison with experimental photoionization cross sections. Generalizations to diatomic molecules in 3D, such as LiH and CO, are currently in progress based on single-particle orbital expansions in prolate spheroidal coordinates.

ACKNOWLEDGMENTS

The authors gratefully thank D. Hochstuhl, H. Miyagi, and M. Bonitz for fruitful discussions. S.B. thanks H. Larsson for helpful comments. This work was supported by the ERC-StG (Project No. 277767-TDMET), the VKR Center of Excellence, QUSCOPE and the BMBF in the frame of the “Verbundprojekt FSP 302.”

APPENDIX A: PARTIAL ROTATION OF THE SINGLE-PARTICLE BASIS

Let us start with the FE-DVR basis functions $\{|\chi_i\rangle\}$, cf. Eqs. (16) and (17), which span the complete simulation region $x \in [0, x_s]$. For simplicity, we consider only $x \geq 0$. For the interval $[-x_s, x_s]$, the basis can be sorted accordingly.

We partition the basis into a central part $i \in [1, N_c]$ and an outer part $i \in [N_c + 1, N_b]$. Because of the orthonormality of the FE-DVR functions, we can expand any wave function in the central and the outer parts,

$$|\Psi(t)\rangle = \underbrace{\sum_{i=1}^{N_c} c_i^c(t) |\chi_i\rangle}_{|\Phi^c(t)\rangle} + \underbrace{\sum_{i=1+N_c}^{N_b} c_i^o(t) |\chi_i\rangle}_{|\Phi^o(t)\rangle}. \quad (\text{A1})$$

Especially, $|\chi_i\rangle \perp |\Phi^o\rangle$ for any $i \leq N_c$.

Consider the unitary basis transform

$$\mathbf{b} = \begin{pmatrix} \mathbf{b}^c & \\ & \mathbf{1} \end{pmatrix}, \quad (\text{A2})$$

which is similar to a rotation of the basis to new basis functions

$$|\phi_\alpha\rangle = \sum_{i=1}^{N_c} \langle \chi_i | \phi_\alpha \rangle |\chi_i\rangle \equiv \sum_{i=1}^{N_c} b_{i\alpha} |\chi_i\rangle, \quad (\text{A3})$$

$$|\chi_i\rangle = \sum_{\alpha=1}^{N_c} \langle \phi_\alpha | \chi_i \rangle |\phi_\alpha\rangle \equiv \sum_{\alpha=1}^{N_c} b_{\alpha i}^* |\phi_\alpha\rangle, \quad (\text{A4})$$

for $\alpha, i \leq N_c$ and $\chi_i \equiv \phi_i$ else.

The rotated wave function can be written, analogously to Eq. (A1), as

$$|\Psi_{\text{rot}}(t)\rangle = |\Phi_{\text{rot}}^c(t)\rangle + |\Phi_{\text{rot}}^o(t)\rangle. \quad (\text{A5})$$

The outer part of the wave function, $|\Phi_{\text{rot}}^o\rangle$, is thus transformed as

$$\begin{aligned} |\Phi_{\text{rot}}^o(t)\rangle &= \sum_{\alpha=N_c+1}^{N_b} \langle \phi_\alpha | \Psi(t) \rangle |\phi_\alpha\rangle \\ &= \sum_{\alpha=N_c+1}^{N_b} \sum_{i,j} \underbrace{\langle \phi_\alpha | \chi_i \rangle}_{\delta_{\alpha i}} \langle \chi_i | \Psi(t) \rangle \underbrace{\langle \chi_j | \phi_\alpha \rangle}_{\delta_{j\alpha}=\delta_{ij}} |\chi_j\rangle \\ &= \sum_{i=N_c+1}^{N_b} \langle \chi_i | \Psi(t) \rangle |\chi_i\rangle \\ &= |\Phi^o\rangle. \end{aligned} \quad (\text{A6})$$

Using a transform of type Eq. (A2), therefore, does not change the outer part of the wave function. The inner part transforms as

$$\begin{aligned} |\Phi_{\text{rot}}^c(t)\rangle &= \sum_{\alpha=1}^{N_c} \langle \phi_\alpha | \Psi(t) \rangle |\phi_\alpha\rangle \\ &= \sum_{\alpha=1}^{N_c} \sum_{i=1}^{N_c} \langle \phi_\alpha | \chi_i \rangle \langle \chi_i | \Psi(t) \rangle |\phi_\alpha\rangle \\ &= \sum_{\alpha=1}^{N_c} \sum_{i=1}^{N_c} b_{\alpha i}^* c_i(t) |\phi_\alpha\rangle. \end{aligned} \quad (\text{A7})$$

Thus, for the central region, $\alpha, i < N_c$, the coefficient vector c_i is transformed to the rotated basis, which is a standard technique in quantum chemistry calculations.

Of course, only the single-particle wave function is invariant under such rotations (and so is the FCI many-particle wave function). For truncated CI expansion this is not true, because the truncation error depends on the accuracy of the single-particle orbitals. Therefore, the best unitary transformation matrix with the constraint of the boundary at the central and the outer region has to be found. Up to now, no straightforward method to determine this matrix for arbitrary TD problems is available; thus, the choice of the transformation matrix \mathbf{b} is guided by physical and mathematical intuition.

APPENDIX B: TRANSFORMATION AND STORAGE OF ELECTRON INTEGRALS

A crucial part for the numerical performance of TD-GASCI calculations is the efficient transformation and storage of the one- and two-electron matrix elements from the FE-DVR to the partially rotated basis. Extending ideas from [46], we evaluate the transformations analytically by exploiting the δ structure of the FE-DVR matrix elements and the transformation matrix \mathbf{b} which results in fast transformations and offers a strategy for the efficient storage of the transformed integrals. Similar strategies can be applied for 3D spherical coordinates and prolate spheroidal coordinates.

1. Transformation of one-electron integrals

Let $\langle i|$ and $|j\rangle$ be basis functions from the original FE-DVR set, i.e., with analytically known matrix elements $h_{ij} = \langle i|h|j\rangle$ of the single-particle part h of the Hamiltonian. Let $\langle\alpha|$ and $|\beta\rangle$ denote the rotated mixed basis set, which can be expanded in the FE-DVR basis as

$$\langle\alpha| = \sum_{i=1}^{N_b} b_{\alpha i}^* \langle i| \quad \text{and} \quad |\beta\rangle = \sum_{j=1}^{N_b} b_{\beta j} |j\rangle. \quad (\text{B1})$$

The transformation matrix from the FE-DVR basis $|i\rangle$ to the mixed basis $|\alpha\rangle$ is given by Eq. (A2), i.e., for $i, \alpha \in [1, N_c]$, $b_{\alpha, i}$ corresponds to the expansion coefficients of the pseudo-orbitals in the FE-DVR set, and when $i, \alpha > N_H$ $b_{\alpha, i}$ is diagonal, $b_{\alpha, i} \equiv \delta_{\alpha, i}$. The latter case corresponds to the situation $|\beta\rangle = |j\rangle$ and $\langle\alpha| = \langle i|$ outside the central region.

The task is to find the matrix elements of h in the new basis, i.e., $\langle\alpha|h|\beta\rangle \equiv h_{\alpha, \beta}$. Using Eq. (B1), we straightforwardly arrive at

$$h_{\alpha\beta} = \sum_{i=1}^{N_b} \sum_{j=1}^{N_b} b_{\alpha i}^* \langle i|h|j\rangle b_{\beta j}. \quad (\text{B2})$$

For numerical performance [46,96], at the cost of slightly increased memory consumption, it is favorable to split this transformation into two parts with a temporary matrix h^1 :

$$\begin{aligned} h_{i\beta}^1 &= \sum_{j=1}^{N_b} b_{\beta j} h_{ij}, \\ h_{\alpha\beta} &= \sum_{i=1}^{N_b} b_{\alpha i}^* h_{i\beta}^1. \end{aligned} \quad (\text{B3})$$

These results can be further simplified by exploiting the diagonal structure of the transformation matrix \mathbf{b} for $\alpha, i > N_c$, cf. Eq. (A2),

$$\begin{aligned} h_{i\beta}^1 &= \underbrace{\sum_{j=1}^{N_c} b_{\beta j} h_{ij}}_{\text{if } \beta \leq N_c, 0 \text{ else}} + \underbrace{h_{i\beta}}_{\text{if } \beta > N_c, 0 \text{ else}}, \\ h_{\alpha\beta} &= \underbrace{\sum_{j=1}^{N_c} b_{\alpha j}^* h_{j\beta}^1}_{\text{if } \beta \leq N_c, 0 \text{ else}} + \underbrace{h_{\alpha\beta}^1}_{\text{if } \alpha > N_c, 0 \text{ else}}. \end{aligned} \quad (\text{B4})$$

Additional straightforward use of symmetry properties of the FE-DVR matrix elements, such as the diagonal or banded structure of the kinetic and the potential energies, reduces the computational and memory costs further.

2. Transformation of two-electron integrals

For the four-indexed two-electron integrals w_{ijkl} , we use a similar approach. Here the transformation is split into three parts [46,96]. Greek letters $\alpha, \beta, \gamma, \delta$ denote transformed indices; Latin letters i, j, k, l correspond to the untransformed FE-DVR basis:

$$(1) \quad w_{ijkl} \rightarrow w_{ij\gamma\delta}^{(1)},$$

$$w_{ij\gamma\delta}^{(1)} = \sum_{k=1}^{N_b} b_{\gamma k}^* \sum_{l=1}^{N_b} b_{\delta l} w_{ijkl}; \quad (\text{B5})$$

$$(2) \quad w_{ij\gamma\delta}^{(1)} \rightarrow w_{i\beta\gamma\delta}^{(2)},$$

$$w_{i\beta\gamma\delta}^{(2)} = \sum_j b_{\beta j} w_{ij\gamma\delta}^{(1)}; \quad (\text{B6})$$

$$(3) \quad w_{i\beta\gamma\delta}^{(2)} \rightarrow w_{\alpha\beta\gamma\delta}^{(m)},$$

$$w_{\alpha\beta\gamma\delta}^{(m)} = \sum_{i=1}^{N_b} b_{\alpha i}^* w_{i\beta\gamma\delta}^{(2)}. \quad (\text{B7})$$

Due to the special structure of the transformation matrix $b_{\alpha i}$, which is $\delta_{\alpha i}$ for $\alpha, i > N_c$ and the structure of the FE-DVR matrix elements $w_{ijkl} \propto \delta_{ij} \delta_{kl}$, the above transformations (B5)–(B7) can be simplified (w_{ik}^F denotes the diagonal FE-DVR interaction $w_{ik}^F = w_{ijkl} \delta_{ij} \delta_{kl}$),

$$w_{ij\gamma\delta}^{(1)} = \begin{cases} \delta_{ij} \sum_{k=1}^{N_c} b_{\gamma k}^* b_{\delta k} w_{ik}^F & \gamma, \delta \leq N_c, \\ \delta_{ij} \delta_{\gamma\delta} w_{i\gamma}^F & \gamma, \delta > N_c, \\ 0 & \text{else,} \end{cases} \quad (\text{B8})$$

which can be decomposed into a central part $w_{i\beta\gamma\delta}^{(1C)} = \sum_k b_{\gamma k}^* b_{\delta k} w_{ik}^F$ of dimension $N_b \times N_c \times N_c$ and a diagonal part, which corresponds to the FE-DVR matrix elements and does not need to be stored.

The second transformation evaluates to

$$w_{i\beta\gamma\delta}^{(2)} = \begin{cases} b_{\beta i} w_{i\gamma\delta}^{(1C)} & i, \beta, \gamma, \delta \leq N_c, \\ b_{\beta i} w_{i\gamma}^F \delta_{\gamma\delta} & \gamma, \delta > N_c; i, \beta \leq N_c, \\ b_{\beta i} w_{i\gamma\delta}^{(1C)} \delta_{\beta i} & \gamma, \delta \leq N_c; i, \beta > N_c, \\ w_{i\gamma}^F \delta_{i\beta} \delta_{\gamma\delta} & i, \beta, \gamma, \delta > N_c, \end{cases} \quad (\text{B9})$$

which gives a central four-indexed part $w_{i\beta\gamma\delta}^{(2C)}$ of dimension $N_c \times N_c \times N_c \times N_c$, two ‘‘mixed’’ parts $w^{(2F1)}$ and $w^{(2F2)}$ of dimension $N_c \times N_c \times N_F$, with $N_F = (N_b - N_c)$, and the ‘‘outer’’ diagonal part, which again corresponds to the FE-DVR matrix elements.

The transformation can be simplified to

$$w_{\alpha,\beta,\gamma,\delta}^{(m)} = \begin{cases} \sum_{i=1}^{N_c} b_{ai}^* w_{i\beta\gamma\delta}^{(2C)} & \alpha, \beta, \gamma, \delta \leq N_c, \\ \delta_{\gamma\delta} \sum_{i=1}^{N_c} b_{ai}^* w_{i\beta\gamma}^{(2F1)} & \alpha, \beta \leq N_c; \gamma, \delta > N_c, \\ w_{\alpha\gamma\delta}^{(2F2)} \delta_{\alpha\beta} & \alpha, \beta > N_c; \gamma, \delta \leq N_c, \\ \delta_{\alpha\beta} \delta_{\gamma\delta} w_{\alpha\gamma}^F & \alpha, \beta, \gamma, \delta > N_c. \end{cases} \quad (\text{B10})$$

Assuming real-valued orbitals, such as the FE-DVR functions in 1D, the symmetry relation for the two-electron

integrals, $w_{\alpha\beta,\gamma\delta} = w_{\gamma\delta,\alpha\beta}$, reduces the storage requirements to $w_{\alpha\beta,\gamma\delta}^C$ [first row of Eq. (B10)] and either w^{F1} or w^{F2} [second or third row of Eq. (B10)]. Thus, in total two arrays have to be stored. The central array $w_{\alpha,\beta,\gamma,\delta}^H$ for $\alpha, \beta, \gamma, \delta \leq N_H$ of dimension $N_c \times N_c \times N_c \times N_c$ and one mixed, three-indexed, array $w_{\alpha,\gamma,\delta}^{F1}$ or $w_{\alpha,\beta,\gamma}^{F2}$ of dimension $N_F \times N_c \times N_c$. This allows for an efficient storage scheme of the two-electron integrals in the mixed basis set approach and with that for the application of GASCI to large extended systems (e.g., photoionization) without approximation of the interaction matrix elements.

-
- [1] T. Brabec and F. Krausz, *Rev. Mod. Phys.* **72**, 545 (2000).
[2] F. Krausz and M. Ivanov, *Rev. Mod. Phys.* **81**, 163 (2009).
[3] B. Schütte, S. Bauch, U. Fröhling, M. Wieland, M. Gensch, E. Plönjes, T. Gaumnitz, A. Azima, M. Bonitz, and M. Drescher, *Phys. Rev. Lett.* **108**, 253003 (2012).
[4] S. Bauch and M. Bonitz, *Phys. Rev. A* **85**, 053416 (2012).
[5] K. C. Kulander, *Phys. Rev. A* **35**, 445 (1987).
[6] P. Krause, T. Klamroth, and P. Saalfrank, *J. Chem. Phys.* **123**, 074105 (2005).
[7] N. Rohringer, A. Gordon, and R. Santra, *Phys. Rev. A* **74**, 043420 (2006).
[8] F. Wilken and D. Bauer, *Phys. Rev. A* **76**, 023409 (2007).
[9] M. Brics and D. Bauer, *Phys. Rev. A* **88**, 052514 (2013).
[10] S. Kvaal, *J. Chem. Phys.* **136**, 194109 (2012).
[11] K. Balzer, S. Bauch, and M. Bonitz, *Phys. Rev. A* **81**, 022510 (2010).
[12] K. Balzer, S. Bauch, and M. Bonitz, *Phys. Rev. A* **82**, 033427 (2010).
[13] D. Hochstuhl, S. Bauch, and M. Bonitz, *J. Phys.: Conf. Ser.* **220**, 012019 (2010).
[14] M. Schultze, M. Fieß, N. Karpowicz, J. Gagnon, M. Korbman, M. Hofstetter, S. Neppl, A. L. Cavalieri, Y. Komninos, Th. Mercouris, C. A. Nicolaides, R. Pazourek, S. Nagele, J. Feist, J. Burgdörfer, A. M. Azzeer, R. Ernstorfer, R. Kienberger, U. Kleineberg, E. Goulielmakis, F. Krausz, and V. S. Yakovlev, *Science* **328**, 1658 (2010).
[15] T. Mercouris, Y. Komninos, and C. A. Nicolaides, *Adv. Quantum Chemistry* **60**, 333 (2010).
[16] H. W. van der Hart, M. A. Lysaght, and P. G. Burke, *Phys. Rev. A* **76**, 043405 (2007).
[17] M. A. Lysaght, P. G. Burke, and H. W. van der Hart, *Phys. Rev. Lett.* **101**, 253001 (2008).
[18] M. A. Lysaght, H. W. van der Hart, and P. G. Burke, *Phys. Rev. A* **79**, 053411 (2009).
[19] H. W. van der Hart, *Phys. Rev. A* **89**, 053407 (2014).
[20] D. Hochstuhl and M. Bonitz, *J. Chem. Phys.* **134**, 084106 (2011).
[21] J. Caillat, J. Zanghellini, M. Kitzler, O. Koch, W. Kreuzer, and A. Scrinzi, *Phys. Rev. A* **71**, 012712 (2005).
[22] M. Nest, T. Klamroth, and P. Saalfrank, *J. Chem. Phys.* **122**, 124102 (2005).
[23] T. Kato and H. Kono, *Chem. Phys. Lett.* **392**, 533 (2004).
[24] H.-D. Meyer, U. Manthe, and L. S. Cederbaum, *Chem. Phys. Lett.* **165**, 73 (1990).
[25] D. J. Haxton, K. V. Lawler, and C. W. McCurdy, *Phys. Rev. A* **86**, 013406 (2012).
[26] T. Sato and K. L. Ishikawa, *Phys. Rev. A* **88**, 023402 (2013).
[27] H. Miyagi and L. B. Madsen, *Phys. Rev. A* **87**, 062511 (2013).
[28] H. Miyagi and L. B. Madsen, *J. Chem. Phys.* **140**, 164309 (2014).
[29] H. Miyagi and L. B. Madsen, *Phys. Rev. A* **89**, 063416 (2014).
[30] J. Olsen, B. O. Roos, P. Jørgensen, and H. J. Aa. Jensen, *J. Chem. Phys.* **89**, 2185 (1988).
[31] T. Fleig, J. Olsen, and C. M. Marian, *J. Chem. Phys.* **114**, 4775 (2001).
[32] D. Hochstuhl and M. Bonitz, *Phys. Rev. A* **86**, 053424 (2012).
[33] D. Hochstuhl and M. Bonitz, *J. Phys.: Conf. Ser.* **427**, 012007 (2013).
[34] J. L. Krause, K. J. Schafer, and K. C. Kulander, *Phys. Rev. A* **45**, 4998 (1992).
[35] K. C. Kulander, K. J. Schafer, and J. L. Krause, *Int. J. Quantum Chem.* **40**, 415 (1991).
[36] K. J. Schafer, B. Yang, L. F. DiMauro, and K. C. Kulander, *Phys. Rev. Lett.* **70**, 1599 (1993).
[37] K. T. Taylor, J. S. Parker, D. Dundas, K. J. Meharg, B. J. S. Doherty, D. S. Murphy, and J. F. McCann, *J. Electron. Spectrosc. Relat. Phenom.* **144-147**, 1191 (2005).
[38] J. S. Parker, B. J. S. Doherty, K. T. Taylor, K. D. Schultz, C. I. Blaga, and L. F. DiMauro, *Phys. Rev. Lett.* **96**, 133001 (2006).
[39] R. Nepstad, T. Birkeland, and M. Førre, *Phys. Rev. A* **81**, 063402 (2010).
[40] A. S. Simonsen, S. A. Sørngård, R. Nepstad, and M. Førre, *Phys. Rev. A* **85**, 063404 (2012).
[41] S. Laulan and H. Bachau, *Phys. Rev. A* **68**, 013409 (2003).
[42] J. Colgan and M. S. Pindzola, *Phys. Rev. Lett.* **88**, 173002 (2002).
[43] R. Pazourek, J. Feist, S. Nagele, and J. Burgdörfer, *Phys. Rev. Lett.* **108**, 163001 (2012).
[44] J. Feist, S. Nagele, R. Pazourek, E. Persson, B. I. Schneider, L. A. Collins, and J. Burgdörfer, *Phys. Rev. A* **77**, 043420 (2008).
[45] J. Feist, S. Nagele, R. Pazourek, E. Persson, B. I. Schneider, L. A. Collins, and J. Burgdörfer, *Phys. Rev. Lett.* **103**, 063002 (2009).
[46] D. Hochstuhl, C. M. Hinz, and M. Bonitz, *Eur. Phys. J. Spec. Top.* **223**, 177 (2014).
[47] T. Helgaker, P. Jørgensen, and J. Olsen, *Molecular Electronic Structure Theory* (Wiley, Chichester, UK, 2000).

- [48] J. Olsen, P. Jørgensen, and J. Simons, *Chem. Phys. Lett.* **169**, 463 (1990).
- [49] Z. Gan and R. J. Harrison, Supercomputing, *Proceedings of the ACM/IEEE SC 2005 Conference* (IEEE, Piscataway, NJ, 2005).
- [50] A. Gordon, F. X. Kärtner, N. Rohringer, and R. Santra, *Phys. Rev. Lett.* **96**, 223902 (2006).
- [51] P. Krause, T. Klamroth, and P. Saalfrank, *J. Chem. Phys.* **127**, 034107 (2007).
- [52] S. Klinkusch, P. Saalfrank, and T. Klamroth, *J. Chem. Phys.* **131**, 114304 (2009).
- [53] N. Rohringer and R. Santra, *Phys. Rev. A* **79**, 053402 (2009).
- [54] S. Pabst and R. Santra, *Phys. Rev. Lett.* **111**, 233005 (2013).
- [55] A. Karamatskou, S. Pabst, Y.-J. Chen, and R. Santra, *Phys. Rev. A* **89**, 033415 (2014).
- [56] L. Greenman, P. J. Ho, S. Pabst, E. Kamarchik, D. A. Mazziotti, and R. Santra, *Phys. Rev. A* **82**, 023406 (2010).
- [57] E. Luppi and M. Head-Gordon, *Mol. Phys.* **110**, 909 (2012).
- [58] D. Cremer, *WIREs Comput. Mol. Sci.* **3**, 482 (2013).
- [59] F. Jensen, *Introduction to Computational Chemistry* (Wiley, Chichester, 2007).
- [60] L. K. Sørensen, T. Fleig, and J. Olsen, *Z. Phys. Chem.* **224**, 671 (2010).
- [61] L. K. Sørensen, J. Olsen, and T. Fleig, *J. Chem. Phys.* **134**, 214102 (2011).
- [62] L. K. Sørensen, S. Bauch, and L. B. Madsen (unpublished).
- [63] T. J. Park and J. C. Light, *J. Chem. Phys.* **85**, 5870 (1986).
- [64] M. H. Beck, A. Jäckle, G. A. Worth, and H.-D. Meyer, *Phys. Rep.* **324**, 1 (2000).
- [65] R. Kosloff and H. Tal-Ezer, *Chem. Phys. Lett.* **127**, 223 (1986).
- [66] D. Bauer and P. Koval, *Comp. Phys. Commun.* **174**, 396 (2006).
- [67] A. Szabo and N. S. Ostlund, *Modern Quantum Chemistry* (reprint) (Dover, Mineola, NY, 1996).
- [68] We prefer the term “partially rotated” in contrast to “mixed” basis used in Ref. [32] since the underlying FE-DVR basis spans the whole grid and only parts of it are rotated. Frequently, the term “mixed basis” is also used for radial grids in combination with angular eigenfunctions [37].
- [69] L. Tao, C. W. McCurdy, and T. N. Rescigno, *Phys. Rev. A* **79**, 012719 (2009).
- [70] F. L. Yip, F. Martín, C. W. McCurdy, and T. N. Rescigno, *Phys. Rev. A* **84**, 053417 (2011).
- [71] T. N. Rescigno and C. W. McCurdy, *Phys. Rev. A* **62**, 032706 (2000).
- [72] H. Bachau, E. Cormier, P. Decleva, J. E. Hansen, and F. Martin, *Rep. Prog. Phys.* **64**, 1815 (2001).
- [73] K. Balzer, S. Bauch, and M. Bonitz, *J. Phys.: Conf. Ser.* **220**, 012020 (2010).
- [74] B. I. Schneider, L. A. Collins, and S. X. Hu, *Phys. Rev. E* **73**, 036708 (2006).
- [75] L. R. Moore, M. A. Lysaght, J. S. Parker, H. W. van der Hart, and K. T. Taylor, *Phys. Rev. A* **84**, 061404(R) (2011).
- [76] P.-O. Löwdin, *Phys. Rev.* **97**, 1474 (1955).
- [77] L. B. Madsen, L. A. A. Nikolopoulos, T. K. Kjeldsen, and J. Fernandez, *Phys. Rev. A* **76**, 063407 (2007).
- [78] L. Argenti, R. Pazourek, J. Feist, S. Nagele, M. Liertzer, E. Persson, J. Burgdörfer, and E. Lindroth, *Phys. Rev. A* **87**, 053405 (2013).
- [79] S. L. Haan, R. Grobe, and J. H. Eberly, *Phys. Rev. A* **50**, 378 (1994).
- [80] S. Bauch, K. Balzer, and M. Bonitz, *Europhys. Lett.* **91**, 53001 (2010).
- [81] M. S. Pindzola, D. C. Griffin, and C. Bottcher, *Phys. Rev. Lett.* **66**, 2305 (1991).
- [82] M. Ruggenthaler and D. Bauer, *Phys. Rev. Lett.* **102**, 233001 (2009).
- [83] E. W. Weisstein, “Blackman Function,” from MathWorld—A Wolfram Web Resource, <http://mathworld.wolfram.com/BlackmanFunction.html>.
- [84] O. I. Tolstikhin, T. Morishita, and L. B. Madsen, *Phys. Rev. A* **84**, 053423 (2011).
- [85] L. Holmegaard, J. L. Hansen, L. Kalthøj, S. L. Kragh, H. Stapelfeldt, F. Filsinger, J. Kuepper, G. Meijer, D. Dimitrovski, M. Abu-samha *et al.*, *Nat. Phys. (London)* **6**, 428 (2010).
- [86] D. Dimitrovski, M. Abu-samha, L. B. Madsen, F. Filsinger, G. Meijer, J. Kupper, L. Holmegaard, L. Kalthøj, J. H. Nielsen, and H. Stapelfeldt, *Phys. Rev. A* **83**, 023405 (2011).
- [87] L. B. Madsen, F. Jensen, O. I. Tolstikhin, and T. Morishita, *Phys. Rev. A* **87**, 013406 (2013).
- [88] H. Ohmura, N. Saito, and T. Morishita, *Phys. Rev. A* **89**, 013405 (2014).
- [89] J. L. Hansen, L. Holmegaard, J. H. Nielsen, H. Stapelfeldt, D. Dimitrovski, and L. B. Madsen, *J. Phys. B* **45**, 015101 (2012).
- [90] H. Ohmura, N. Saito, and T. Morishita, *Phys. Rev. A* **83**, 063407 (2011).
- [91] H. Li, D. Ray, S. De, I. Znakovskaya, W. Cao, G. Laurent, Z. Wang, M. F. Kling, A. T. Le, and C. L. Cocke, *Phys. Rev. A* **84**, 043429 (2011).
- [92] J. Wu, L. P. H. Schmidt, M. Kunitski, M. Meckel, S. Voss, H. Sann, H. Kim, T. Jahnke, A. Czasch, and R. Dörner, *Phys. Rev. Lett.* **108**, 183001 (2012).
- [93] L. B. Madsen, O. I. Tolstikhin, and T. Morishita, *Phys. Rev. A* **85**, 053404 (2012).
- [94] B. Zhang, J. Yuan, and Z. Zhao, *Phys. Rev. Lett.* **111**, 163001 (2013).
- [95] O. I. Tolstikhin, L. B. Madsen, and T. Morishita, *Phys. Rev. A* **89**, 013421 (2014).
- [96] C. F. Bender, *Comput. Phys.* **9**, 547 (1972).